Northumbria Research Link

Citation: Haseloff, Marianne and Sergienko, Olga V. (2022) Effects of calving and submarine melting on steady states and stability of buttressed marine ice sheets. Journal of Glaciology, 68 (272). pp. 1149-1166. ISSN 0022-1430

Published by: International Glaciological Society

URL: https://doi.org/10.1017/jog.2022.29 <https://doi.org/10.1017/jog.2022.29>

This version was downloaded from Northumbria Research Link: https://nrl.northumbria.ac.uk/id/eprint/48709/

Northumbria University has developed Northumbria Research Link (NRL) to enable users to access the University's research output. Copyright © and moral rights for items on NRL are retained by the individual author(s) and/or other copyright owners. Single copies of full items can be reproduced, displayed or performed, and given to third parties in any format or medium for personal research or study, educational, or not-for-profit purposes without prior permission or charge, provided the authors, title and full bibliographic details are given, as well as a hyperlink and/or URL to the original metadata page. The content must not be changed in any way. Full items must not be sold commercially in any format or medium without formal permission of the copyright holder. The full policy is available online: http://nrl.northumbria.ac.uk/policies.html

This document may differ from the final, published version of the research and has been made available online in accordance with publisher policies. To read and/or cite from the published version of the research, please visit the publisher's website (a subscription may be required.)

Northumbria University NEWCASTLE

University Library

Journal of Glaciology

Article

Cite this article: Haseloff M, Sergienko OV (2022). Effects of calving and submarine melting on steady states and stability of buttressed marine ice sheets. *Journal of Glaciology* **68**(272), 1149–1166. https://doi.org/10.1017/jog.2022.29

Received: 22 October 2021
Revised: 17 March 2022
Accepted: 18 March 2022
First published online: 23 May 2022

Keywords:
Calving; ice dynamics; ice/ocean interactions; ice-sheet modelling; ice shelves

Author for correspondence:
Marianne Haseloff,
E-mail: marianne.haseloff@northumbria.ac.uk

© The Author(s), 2022. Published by Cambridge University Press. This is an Open Access article, distributed under the terms of the Creative Commons Attribution licence (https://creativecommons.org/licenses/by/4.0/), which permits unrestricted re-use, distribution, and reproduction in any medium, provided the original work is properly cited.

cambridge.org/jog

Effects of calving and submarine melting on steady states and stability of buttressed marine ice sheets

Marianne Haseloff[1] and Olga V. Sergienko[2]

[1]Geography and Environmental Sciences, Northumbria University, Newcastle upon Tyne, UK and [2]Atmospheric and Oceanic Sciences, Princeton University, Princeton, NJ, USA

Abstract

Mass loss from ice shelves is a strong control on grounding-line dynamics. Here we investigate how calving and submarine melt parameterizations affect steady-state grounding-line positions and their stability. Our results indicate that different calving laws with the same melt parameterization result in more diverse steady-state ice-sheet configurations than different melt parameterizations with the same calving law. We show that the backstress at the grounding line depends on the integrated ice-shelf mass flux. Consequently, ice shelves are most sensitive to high melt rates in the vicinity of their grounding lines. For the same shelf-averaged melt rates, different melt parameterizations can lead to very different ice-shelf configurations and grounding-line positions. If the melt rate depends on the slope of the ice-shelf draft, then the positive feedback between increased melting and steepening of the slope can lead to singular melt rates at the ice-shelf front, producing an apparent lower limit of the shelf front thickness as the ice thickness vanishes over a small boundary layer. Our results illustrate that the evolution of marine ice sheets is highly dependent on ice-shelf mass loss mechanisms, and that existing parameterizations can lead to a wide range of modelled grounding-line behaviours.

1. Introduction

Increased mass loss from marine-terminating outlet glaciers in Greenland and Antarctica is usually attributed to warming ocean waters (Holland and others, 2008; Joughin and others, 2010; Pritchard and others, 2012; Straneo and Heimbach, 2013). Key for linking ocean warming and glacier retreat is the buttressing effect of ice shelves, which transmit changes in ocean forcing to the grounded ice. Modelling studies investigating the dynamics of buttressed marine ice sheets have shown that laterally confined ice shelves can suppress a possible instability of marine ice sheets on retrograde slopes (Hughes, 1973; Mercer, 1978; Dupont and Alley, 2005; Schoof, 2007a; Goldberg and others, 2009; Gudmundsson and others, 2012; Gudmundsson, 2013; Pegler, 2018b). Consequently, a reduction of the ice-shelf buttressing caused, for example, by submarine melting might trigger instability (Mercer, 1978), and the grounding-line retreat simulated in large-scale ice-sheet models under projected ocean warming conditions (e.g. Joughin and others, 2014; Robel and others, 2019; Rosier and others, 2021) is often interpreted as a manifestation of this instability.

The marine ice-sheet instability, first proposed by Weertman (1974), is the consequence of a monotonic dependence of the ice flux at the grounding line on ice thickness, which is in turn linked to the depth of the sea floor through the floatation condition (Weertman, 1974; Thomas and Bentley, 1978; Schoof, 2007b). If such a monotonically increasing relationship between flux and ice thickness exists, then retreat of a grounding line onto a deeper sea floor leads to an increase in the ice flux, ice-sheet thinning and continued retreat of the grounding line until a position is reached where the ice flux decreases with further retreat or the ice sheet becomes grounded. Several studies have challenged the simplicity of this picture by demonstrating that a wide range of effects, including ice-shelf buttressing, alters this instability behaviour (e.g. Gomez and others, 2010; Pegler and Worster, 2012; Robel and others, 2014, 2016; Pegler, 2016; Brondex and others, 2017; Sergienko and Wingham, 2019, 2022). However, a systematic investigation of the effects of ice-shelf mass loss processes on the stability of buttressed marine ice sheets is still outstanding.

1.1. Ice-shelf mass loss

Ice shelves lose their mass by two processes: calving of icebergs at the ice-shelf front and submarine melting. Calving is a manifestation of the brittle nature of ice, and modelling individual calving events is beyond the scope of present-day ice-sheet models (e.g. Åström, 2013; Bassis and Jacobs, 2013). Thus, practical approaches to model calving in large-scale ice-sheet models include: (1) fixing the calving front position (e.g., Gudmundsson and others, 2012; Arthern and Williams, 2017), (2) keeping the length of the ice shelf fixed (Gagliardini and others, 2010) and (3) the application of strain-rate-based criteria (e.g. Vieli and others, 2000, 2001; Benn and others, 2007a; Nick and others, 2010; Levermann and others, 2012; Morlighem and others, 2016). In flowline models that do not resolve the flow transverse to the main

https://doi.org/10.1017/jog.2022.29 Published online by Cambridge University Press

flow direction, strain rates at the calving front can be linked to the ice thickness there (Vieli and others, 2000, 2001; Benn and others, 2007a; Nick and others, 2010); these calving criteria have some observational backing (Van der Veen, 1996). However, there is no clear understanding of how the choice of the calving law affects the grounding-line response to external forcing. Here, we aim to address this question by comparing the steady-state grounding-line positions obtained with different calving criteria.

Submarine melting results from the interaction of the ocean circulation with sub-shelf cavities. While fully coupled ice–ocean models are being developed (Goldberg and others, 2012, 2018; De Rydt and Gudmundsson, 2016; Seroussi, 2017; Jordan and others, 2018), the coupling of ice and ocean dynamics remains a major challenge. Such calculations require significant computational resources and detailed knowledge of the ocean conditions (e.g. Goldberg and others, 209) and atmospheric forcing, while at the same time providing complex outputs which make identification of the fundamental feedbacks difficult.

For use in large-scale ice-sheet models, a wide range of submarine melt parameterizations have been proposed. These include an explicit spatial dependence (i.e. a dependence on fixed coordinates (x, y), e.g. Gagliardini and others, 2010; Aschwanden and others, 2019), a dependence on the ice-shelf draft (e.g. Joughin and others, 2010, 2014; Pollard and DeConto, 2012; Favier and others, 2014), or reduced representations of plume dynamics.

Subglacial plume models aim to capture the leading order effects of ice-shelf–ocean interactions caused by buoyant subglacial discharge at the grounding line or buoyant melt water at the ice–ocean interface (e.g. Jenkins, 1991, 2011; Sergienko and others, 2013; Slater and others, 2017; Hewitt, 2020). As this water rises along the ice-shelf face, it entrains sea water. This sea water provides heat to the plume, leading to further melting and increased buoyancy. Crucially, entrainment rates are often assumed to depend on the slope of the ice-shelf base, with larger slopes leading to higher melt rates. The existence of a positive feedback between melting and ice-shelf shape can theoretically explain the formation of undercut ice shelves, and this kind of feedback is explicitly incorporated in models that simulate the evolution of a buoyant plume at the ice-shelf base. Parameterizations of these dynamics typically include a dependence on the slope of the ice-shelf base (e.g. Lazeroms and others, 2018, 2019).

1.2. Study outline

With a diverse range of parameterizations of ice-shelf mass loss it becomes important to develop a basic understanding of how they affect the flow of the grounded ice sheet individually and in different combinations. To build a qualitative understanding, we use simplified representations of these parameterizations to investigate the interaction between submarine melting, calving, ice shelf shape and grounding-line position. From the ice–ocean interaction perspective, our study can be considered complementary to Slater and others (2017), who consider a full plume model and a drastically simplified ice model (by prescribing a fixed ice velocity). In comparison, we use a flowline ice model accounting for both mass and momentum balance, but we use a range of simplified melt parameterizations.

From an ice-dynamics perspective, our study builds on existing work by Schoof and others (2017), Haseloff and Sergienko (2018) and Pegler (2018a, 2018b) who consider different theoretical aspects of buttressed marine ice-sheet dynamics, but generally neglect melting. To do this, we follow the same approach as Schoof (2007b, 2011, 2012), Haseloff and Sergienko (2018) and Sergienko and Wingham (2019, 2022): we derive an expression for the flux at the grounding line, and use it to perform a linear stability analysis. Our results show that the stability criterion derived by Schoof (2012) only holds for sufficiently smooth beds and certain calving laws. Under these conditions, the relationship between the flux gradient and the accumulation rate determines the stability of steady states.

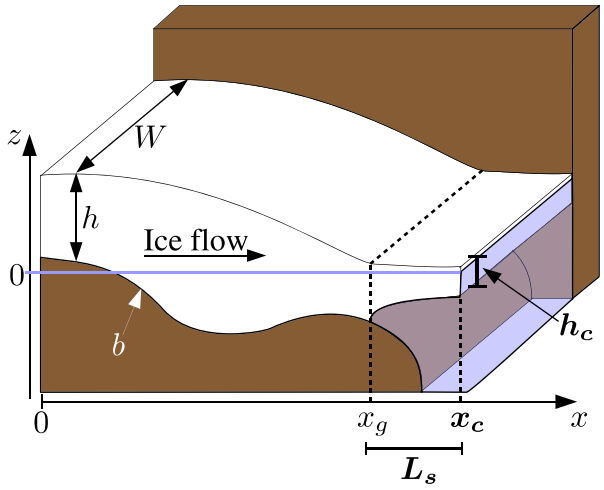

Fig. 1. Cross section of the model.

Like these other models we sacrifice model complexity (and thus applicability) for model tractability by using a flowline model with parameterized side drag. Flowline models cannot account for across-flow variations in geometric properties, flow or melt (e.g. Gudmundsson, 2003; Sergienko, 2012, 2013; Reese and others, 2018a; Zhang and others, 2020). Nevertheless, flowline models have been helpful in developing an understanding of buttressed grounding-line dynamics (Dupont and Alley, 2005; Nick and others, 2010; Hindmarsh, 2012; Jamieson and others, 2012; Pegler and others, 2013; Robel and others, 2014, 2016; Pegler, 2016, 2018a, 2018b; Schoof and others, 2017; Haseloff and Sergienko, 2018, Sergienko, 2022).

The paper is organized as follows: we present the model in Section 2. To build an understanding of the qualitative differences between different melt rate parameterizations, we briefly discuss the response of unconfined ice shelves to these in Section 3, before turning to buttressed marine ice sheets in Section 4. In Section 4.1 we show that different calving laws can render the same steady-state grounding-line position stable or unstable. In Section 4.2 we demonstrate that the buttressed grounding-line flux depends at leading order on the integrated ice flux and illustrate that this results in melting focused closer to the grounding line reducing buttressing more than the same amount of melting applied further away from it. Finally, in Section 4.3 we compare the steady-state grounding-line positions obtained with different melt rate and calving parameterizations, and show that the variability in grounding-line positions due to different calving laws is greater than the variability due to different melt rate parameterizations.

2. The model

We consider a laterally confined marine ice sheet of constant width W flowing in the positive x-direction from an ice divide at $x = 0$ to the calving front at $x = x_c$ (Fig. 1). At the grounding line $x = x_g$ the ice-shelf forms.

2.1. Full model equations

We model the velocity u along the centre line of the ice stream/shelf and the ice thickness h with a widely used laterally averaged

https://doi.org/10.1017/jog.2022.29 Published online by Cambridge University Press

version of a plug flow or 'shallow stream' model (e.g. MacAyeal, 1989; Dupont and Alley, 2005; Nick and others, 2009; Hindmarsh, 2012; Pegler, 2016; Haseloff and Sergienko, 2018)

$$2\frac{\mathrm{d}}{\mathrm{d}x}\left(A^{-1/n}h\left|\frac{\mathrm{d}u}{\mathrm{d}x}\right|^{1/n-1}\frac{\mathrm{d}u}{\mathrm{d}x}\right)-\frac{C_\mathrm{w}A^{-1/n}}{W^{1/n+1}}h|u|^{1/n-1}u - C|u|^{m-1}u-\rho_\mathrm{i}gh\frac{\mathrm{d}(h+b)}{\mathrm{d}x}=0,\quad \text{if } 0<x\le x_\mathrm{g} \tag{1a}$$

$$2\frac{\mathrm{d}}{\mathrm{d}x}\left(A^{-1/n}h\left|\frac{\mathrm{d}u}{\mathrm{d}x}\right|^{1/n-1}\frac{\mathrm{d}u}{\mathrm{d}x}\right)-\frac{C_\mathrm{w}A^{-1/n}}{W^{1/n+1}}h|u|^{1/n-1}u - \rho_\mathrm{i}g\left(1-\frac{\rho_\mathrm{i}}{\rho_\mathrm{w}}\right)h\frac{\mathrm{d}h}{\mathrm{d}x}=0,\quad \text{if } x_\mathrm{g}<x\le x_\mathrm{c} \tag{1b}$$

with the first term in (1a) the divergence of the longitudinal shear stress, the second term the lateral shear stress, the third term the basal shear stress and the last term the driving stress. The parameter A is the rate factor of the ice viscosity, n is a rheology parameter, C_w is a lateral shear stress parameter, ρ_i is the density of ice, ρ_w is the density of water, g is the gravitational constant, m and C are sliding coefficients, and

$$b(x)=100-2184.8\times\left(\frac{x}{155\,\mathrm{km}}\right)^2+1031.72\times\left(\frac{x}{155\,\mathrm{km}}\right)^4-151.72\times\left(\frac{x}{155\,\mathrm{km}}\right)^6 \tag{2}$$

is the elevation of the bed, for which we use a scaled version of the MISMIP and the MISMIP+ bed geometries (Cornford and others, 2020). Parameter values used in this study are listed in Table 1. The equation for mass conservation is

$$\frac{\mathrm{d}(uh)}{\mathrm{d}x}=\begin{cases}\dot{a} & \text{if } 0\le x\le x_\mathrm{g},\\ \dot{m} & \text{if } x_\mathrm{g}<x<x_\mathrm{c}\end{cases} \tag{3}$$

with $\dot{a}$ the net accumulation rate on the ice sheet and $\dot{m}$ the net mass balance term of the ice shelf, combining both surface and basal mass balance contributions (positive: accumulation/freeze-on). We are strictly interested in the effect of changing the ice-shelf mass balance and therefore assume a constant accumulation rate $\dot{a}$ on the grounded ice sheet but different models for the submarine melt rate, given in Eqn (5). To simplify the derivation of asymptotic solutions, we neglect accumulation on the ice shelf; including a constant accumulation term does not change the results qualitatively.

The boundary conditions are

$$\frac{\mathrm{d}(h+b)}{\mathrm{d}x}=u=0\quad\text{at } x=0 \tag{4a}$$

$$h=h_\mathrm{g}=-\frac{\rho_\mathrm{i}}{\rho_\mathrm{w}}b(x_\mathrm{g})\quad\text{at } x=x_\mathrm{g} \tag{4b}$$

$$2A^{-1/n}h\left|\frac{\mathrm{d}u}{\mathrm{d}x}\right|^{1/n-1}\frac{\mathrm{d}u}{\mathrm{d}x}=\frac{1}{2}\rho_\mathrm{i}g\left(1-\frac{\rho_\mathrm{i}}{\rho_\mathrm{w}}\right)h^2\ \text{at } x=x_\mathrm{g}+L_\mathrm{s}. \tag{4c}$$

Additionally, we require the velocity u, the stress (and consequently the velocity gradient $\mathrm{d}u/\mathrm{d}x$), and the ice thickness h to be continuous at the grounding line x_g. To close this model, we still require a condition to describe the length of the ice shelf L_s and a model for the sub-shelf melt rate $\dot{m}$ which we describe next.

2.2. Ice-shelf mass loss

2.2.1 Melting

As direct coupling of ice-sheet models with ocean-circulation models is computationally expensive (e.g. Jordan and others, 2018), a multitude of submarine melt rate parameterizations exist which attempt to capture the relevant processes with either location-dependent parameterizations (e.g. Gagliardini and others, 2010), ice-thickness-dependent parameterizations (e.g. Joughin and others, 2010; Favier and others, 2014) or parameterizations which include a dependence on the ice-shelf slope (e.g. Little and others, 2012; Lazeroms and others, 2018, 2019; Favier and others, 2019).

The focus of this study is to gain insights into the qualitative differences in the grounding-line dynamics resulting from the use of different melt rate parameterizations. We therefore consider a limited subset of idealized parameterizations representative of typical choices:

$$\dot{m}=\begin{cases}f(x)\\ \gamma_2 h^2\\ \gamma_3(h_\mathrm{g}-h)\left|\frac{\mathrm{d}h}{\mathrm{d}x}\right|\frac{1}{\sqrt{1+\epsilon^2(\mathrm{d}h/\mathrm{d}x)^2}},\quad \epsilon\ll 1.\end{cases} \tag{5}$$

The first parameterization assumes a dependence on the downstream coordinate x only, that is, we assume melting to be independent of the ice-shelf thickness h or slope $\mathrm{d}h/\mathrm{d}x$. The second parameterization $(5)_2$ depends on the ice-shelf draft (depth of the ice-shelf base below sea level) and is similar to two parameterizations that have been used in studies of Pine Island (Joughin and others, 2010; Favier and others, 2014). The important assumption underlying this parameterization is that melting increases with depth; consequently, melt rates are largest directly at the grounding line.

The slope-dependent parameterization $(5)_3$ is a strong simplification of the melt rate derived by Lazeroms and others (2018), who derive a general parameterization of the melt rates obtained with a plume model (Jenkins, 1991). In their parameterization, the melt rate is proportional to $\sin\alpha$ where α is the slope of the ice draft, and an 11th-order polynomial in the distance from the grounding line. We include the former dependence through an explicit slope-dependent term $\mathrm{d}h/\mathrm{d}x$, and the latter through the dependence on $(h_\mathrm{g}-h)$. The term $1/\sqrt{1+\epsilon^2(\mathrm{d}h/\mathrm{d}x)^2}$ with $0<\epsilon\ll 1$ is included as regularization of the melt rate in the limit of $\mathrm{d}h/\mathrm{d}x\to\infty$.

2.2.2. Calving

Unless all ice-shelf mass is removed through melting, solution of the ice-flow model (1)–(4) additionally requires a condition that determines the position of the calving front x_c. This is generally done through a calving law, and similarly to melt rate parameterizations, a large range of options exist (e.g. Van der Veen, 1998; Dupont and Alley, 2005; Benn and others, 2007b; Goldberg and others, 2009; Nick and others, 2010; Gagliardini and others, 2010; Jamieson and others, 2012; Gudmundsson and others, 2012).

The most numerically convenient of these choices is the assumption of a fixed calving front position $x_\mathrm{c}=\text{const.}$ (e.g. Gudmundsson and others, 2012; Arthern and Williams, 2017) as this does not require explicitly tracking the movement of the calving front. An alternative class of calving laws is based on stress or ice thickness criteria, effectively prescribing a certain ice thickness at the calving front as extensional stress and ice thickness there are linked through (4c) (e.g. Vieli and others, 2000; Benn and others, 2007a; Nick and others, 2010; Choi and others, 2021). A third calving choice we will consider assumes a fixed ice-shelf length, i.e. assuming $x_\mathrm{c}=x_\mathrm{g}+L_0$ with $L_0=\text{const.}$ While this choice would be computationally difficult to implement in

https://doi.org/10.1017/jog.2022.29 Published online by Cambridge University Press

laterally extended numerical ice-sheet models, it is particularly suitable for our investigation of the roles of melting and calving on grounding-line dynamics through a simplified flowline model as it does not introduce dynamical feedbacks through a varying ice-shelf length.

To summarize, the position of the calving front is here set through:

$$x_c = \begin{cases} x_g + L_0 & \text{where } L_0 = \text{const.} \\ \text{const.} & \\ x^\dagger & \text{where } h(x^\dagger) = h_c = \text{const.} \end{cases} \tag{6}$$

with the first option describing a constant ice-shelf length L_0, the second option describing a constant calving front position x_c, and the third option describing a constant ice thickness at the calving front h_c. Note however that in the case of strong melting it is possible for the ice thickness to go to zero before this location in which case the ice-shelf length is set by the location where h goes to zero. The length of the ice shelf is thus given by

$$L_s = \min\left(x_c - x_g, x^* - x_g\right) \quad \text{with} \quad h(x^*) = 0. \tag{7}$$

2.3 Reduced model equations

In the grounded part of the marine ice-sheet longitudinal stress gradients can be neglected in the momentum balance and the above problem can be described by a reduced model (Schoof, 2007b; Haseloff and Sergienko, 2018; Sergienko and Wingham, 2022):

$$-\frac{C_w A^{-1/n}}{W^{1/n+1}} h|u|^{1/n-1}u - C|u|^{m-1}u - \rho_i g h \frac{\mathrm{d}(h+b)}{\mathrm{d}x} = 0, \quad \text{if } 0 < x \le x_g \tag{8a}$$

$$\frac{\mathrm{d}q}{\mathrm{d}x} = \frac{\mathrm{d}(uh)}{\mathrm{d}x} = \dot{a}, \quad \text{if } 0 < x \le x_g. \tag{8b}$$

This is essentially a 'shallow ice' model (Fowler and Larson, 1978; Morland and Johnson, 1980), and the boundary conditions of this system are:

$$\frac{\mathrm{d}(h+b)}{\mathrm{d}x} = u = 0 \qquad \text{at } x = 0 \tag{9a}$$

$$h = h_g = -\frac{\rho_i}{\rho_w} b(x_g) \qquad \text{at } x = x_g \tag{9b}$$

$$uh = q_g \qquad \text{at } x = x_g. \tag{9c}$$

with (9c) effectively replacing the stress boundary condition (4c) (see, e.g. Schoof, 2007b, for details). It is straightforward to see that for the steady-state problems considered here, the flux at grounding line has to match the integrated mass balance (8b):

$$q_g = \int_0^{x_g} \dot{a}\, \mathrm{d}x. \tag{10}$$

Determining an expression for the flux at the grounding line therefore closes the reduced system.

2.3.1 Grounding-line flux

If the longitudinal stress gradient is small at the grounding line, an expression for the ice flux can be derived from the continuity condition of the stress at the grounding line (see e.g. Hindmarsh, 2012; Sergienko and Wingham, 2022), i.e.

$$\tau_{\text{stream}} = \tau_{\text{shelf}} \quad \text{at} \quad x = x_g, \tag{11a}$$

where

$$\tau_{\text{stream}} = \frac{2}{A^{1/n}} h \left|\frac{\mathrm{d}u}{\mathrm{d}x}\right|^{1/n-1} \frac{\mathrm{d}u}{\mathrm{d}x} \tag{11b}$$

and

$$\tau_{\text{shelf}} = \tau_0 \times \Theta \quad \text{with} \quad \tau_0 = \frac{1}{2}\rho_i g \left(1 - \frac{\rho_i}{\rho_w}\right) h_g^2. \tag{11c}$$

Θ is the ratio between the backstress at the grounding line and the unbuttressed backstress; we discuss its calculation in detail in Section 2.3.2.

From (8a), and reasonably assuming $u > 0$ (i.e. ice flows towards the calving front) and $\mathrm{d}u/\mathrm{d}x > 0$

$$\frac{\mathrm{d}h}{\mathrm{d}x} = -\left[\frac{C_w}{A^{1/n} W^{1/n+1} \rho_i g} u^{1/n} + \frac{C}{\rho_i g}\frac{u^m}{h} + \frac{\mathrm{d}b}{\mathrm{d}x}\right]. \tag{12}$$

Substituting this expression into (11a) and rearranging terms leads to an implicit expression for the ice flux at the grounding line

$$\begin{aligned} &\frac{\mathrm{d}q}{\mathrm{d}x} h^{1/n+m+2} + \frac{C_w}{A^{1/n} W^{1/n+1} \rho_i g} q^{1/n+1} h^{m+1} \\ &\quad + \frac{C}{\rho_i g} q^{m+1} h^{1/n} + q h^{1/n+m+1} \frac{\mathrm{d}b}{\mathrm{d}x} \\ &\quad = \left[\frac{A^{1/n}}{4} \rho_i g \left(1 - \frac{\rho_i}{\rho_w}\right)\right]^n h^{1/n+m+3+n} \Theta^n \end{aligned} \tag{13}$$

where $\mathrm{d}q/\mathrm{d}x$ is determined by (8b) at $x = x_g$; for steady-states $\mathrm{d}q/\mathrm{d}x = \dot{a}$. Note that we only used the momentum balance to determine (13), therefore it is valid for both steady-state and time-evolving problems.

The implicit flux expression (13) contains the flux expression proposed by Schoof (2007a, b)

$$\begin{aligned} q_g &= q_0 \times \Theta^{n/(m+1)} \quad \text{with} \\ q_0 &= \left(\frac{A(\rho_i g)^{n+1}(1 - \rho_i/\rho_w)^n}{4^n C}\right)^{1/(m+1)} h_g^{(3+m+n)/(m+1)} \end{aligned} \tag{14}$$

as a limiting case. Writing (13) in similar form, one can obtain

$$\begin{aligned} q_g &= \frac{q_0}{(1+\Gamma)^{1/(m+1)}} \times \Theta^{n/(m+1)} \quad \text{with} \\ \Gamma &= q_x \frac{\rho_i g}{C} h_g^{m+2} q_g^{-m-1} + \frac{\rho_i g}{C}\frac{\mathrm{d}b}{\mathrm{d}x} h_g^{m+1} q_g^{-m} \\ &\quad + \frac{C_w A^{-1/n}}{C W^{1/n+1}} h_g^{m+1-1/n} q_g^{1/n-m} \end{aligned} \tag{15}$$

with the non-unity parameters in the denominator accounting for the effects of flux gradients (first term in Γ), bed gradients (second term) and lateral shear (third term) on the grounded part, upstream of the grounding line.

We have specifically chosen our model configuration and parameters to satisfy the original assumptions underlying Schoof's asymptotic theory, so that the two expressions (14) and (13) yield almost indistinguishable results in most of the domain. We point out that at the far downstream side of

https://doi.org/10.1017/jog.2022.29 Published online by Cambridge University Press

the bed, past ≈ 300 km, the solutions of (13) cease to exist as the bed slope becomes too large. Mathematically, this is the result of the bracketed term in the denominator of (15) becoming negative in this regime. Consequently, we do not consider configurations with grounding-line positions past this point.

By adopting the grounding-line flux expression (13), we neglect a wide range of dynamic behaviour that is caused by varying basal boundary conditions on the grounded part of the ice sheet (e.g. Tsai and others, 2015; Brondex and others, 2017; Sergienko and Wingham, 2019). We also restrict ourselves to the simplest possible geometry of a laterally confined parallel-sided outlet glacier, as the model considered here is only suitable under such conditions (e.g. Reese and others, 2018b). While this is a clear limitation of our model, neglecting the influence of the basal ice-sheet properties in particular facilitates the interpretation of our results considerably.

2.3.2. Backstress at the grounding line

In either of the flux expressions above Θ must be determined from the ice-shelf equations. In some cases this is possible *analytically*, through construction of asymptotic solutions of the ice-shelf equations (1b) and $(3)_2$ with (10) and (4c), see Appendix B. There we find that the steady-state grounding-line stress for a spatially variable melt rate $\dot{m} = f(x)$ is:

$$\Theta = 1 - \left[\frac{(4^n C_w)^{1/(1+n)} [q(x_c)]^{1/n} + \frac{n+1}{n} \frac{C_w}{W} \int_{x_g}^{x_c} [q(x')]^{1/n} \mathrm{d}x'}{\rho_i g (1 - \rho_i/\rho_w) A^{1/n} W^{1/n} h_g^{1/n+1}} \right]^{2n/(n+1)} \tag{16}$$

with $q(x)$ the steady-state flux on the ice shelf $q(x) = q_g + \int_{x_g}^{x} f(x')\,\mathrm{d}x'$. We discuss this expression in detail in Section 4.2.

As it is not always possible to construct analytical solutions, we also calculate Θ numerically with Matlab ODE solvers. In this case we use a Newton method to determine the backstress τ_{shelf} that simultaneously satisfies the ice-shelf momentum balance (1b) and mass balance condition (3), with boundary conditions (10) and (4c). We refer to this approach as *semi-analytical*.

Finally, verification of our solutions with full numerical solutions of (1)–(7) is obtained with Comsol and an adapted version of the time-dependent grounding-line code described in Schoof (2007a) and Robel and others (2014), which has been extended with an ice-shelf solver to account for buttressing; these solutions are referred to as *numerical* solutions. To summarize, we use three different ways to determine grounding-line position:

(1) analytical solution of (10) and (13) with suitably constructed Θ (e.g. (16), (18) and (25))
(2) semi-analytical solution of (10) and (13) with numerically determined Θ
(3) numerical solution of the full system of equations ((1)–(7)). In this case, the time-dependent mass balance equation

$$\frac{\partial h}{\partial t} + \frac{\partial (uh)}{\partial x} = \dot{a} \quad \text{if } 0 \le x \le x_g$$

is solved instead of $(3)_1$, and the model is run into steady state.

We compare the different approaches in Appendix A and Section 4.2, where we show good agreement between them.

3. Unconfined ice-shelf profiles for different melt rate parameterizations

Before discussing the effect of melting on buttressed marine ice sheets below, we start by considering unconfined ice shelves to build intuition for the interpretation of the buttressed solutions. For an unconfined ice shelf, Eqns (1b) with $(3)_2$ can be solved without recourse to the equations for the grounded ice sheet, if we prescribe the ice flux q and ice thickness h at the grounding line:

$$q = q_g, \quad h = h_g \text{ at } x = x_g. \tag{17}$$

As outlined in the previous section, we additionally need to prescribe the location of the calving front x_c. For an unconfined ice shelf whose grounding-line position is insensitive to the ice-shelf processes, assuming a fixed calving front position or a constant ice-shelf length are identical choices, and we prescribe x_c to be fixed at $x_c = x_g + L_0$. Note however that in the case of strong melting it is possible for the ice thickness to go to zero upstream of this location. In this case x_c is set by the location where h goes to zero. The ice-shelf length L_s is thus given by (7).

Figure 2 shows typical ice-shelf profiles and velocities obtained for the three different melt rate parameterizations given in (5). Each of the parameters γ_1, γ_2 and γ_3 represents a different physical quantity. In order to be able to compare different melt rates, we therefore use the average melt rate on the shelf as reference: profiles plotted in the same colours in panels a_1–c_3 are for the same average melt rates, which are indicated in panels a_4–c_4.

We might expect melt to reduce the ice thickness until it goes to zero at the ice-shelf front, at which point the ice shelf starts to shorten. The solutions for a constant melt rate (column a) indeed exhibit this behaviour, with the ice-shelf shortening once $\gamma_1 < -q_g/L_0$. However, for the second melt rate ($\dot{m} = \gamma_2 h^2$, column b) the ice thickness at the calving front can never reach zero, and the ice shelf thins most close to the grounding line and subsequently maintains an almost constant ice thickness towards the calving front. For this parameterization the average melt rate cannot exceed $-q_g/L_0$, and as this limit is approached for $\gamma_2 \to -\infty$, the ice thickness at the calving front asymptotically approaches zero (Fig. $2b_4$).

The third melt rate parameterization exhibits yet another behaviour (Fig. 2c): the ice shelf appears to retreat before the ice thickness at the shelf front reaches zero and there appears to be a lower bound on the ice thickness at the ice-shelf front (Fig. $2c_4$). Closer examination of these solutions (Appendix B.1) shows that this is only an apparent lower bound: for γ_3 less than a critical γ_c, the melt rate at the ice-shelf front goes to $-1/\epsilon$, so that the ice thickness goes to zero in a small boundary layer of length $O(\epsilon)$ (see 8d–f), with ϵ the regularization parameter in (5).

These examples illustrate that using different melt rate parameterizations leads to very different ice-shelf profiles. With a constant melt rate, the ice shelf becomes almost triangular in the limit of strong melting. Conversely, the ice-thickness dependent melt rate leads to a shape that quickly thins away from the grounding line, as melting is strongest there. When we account for the positive feedback between submarine melt and slope, the ice shelf only thins up to a critical value given in Eqn (B7), beyond which the ice shelf retreats with an seemingly non-zero ice thickness at the ice-shelf front.

Melting affects not only the ice thickness, but also the velocity, as for example illustrated by the velocity profiles in Figure $2a_2$: as melting increases the velocity decreases towards the ice-shelf front compared to solutions with weaker melting. This is a consequence of melting reducing the ice flux, not only the ice thickness in

https://doi.org/10.1017/jog.2022.29 Published online by Cambridge University Press

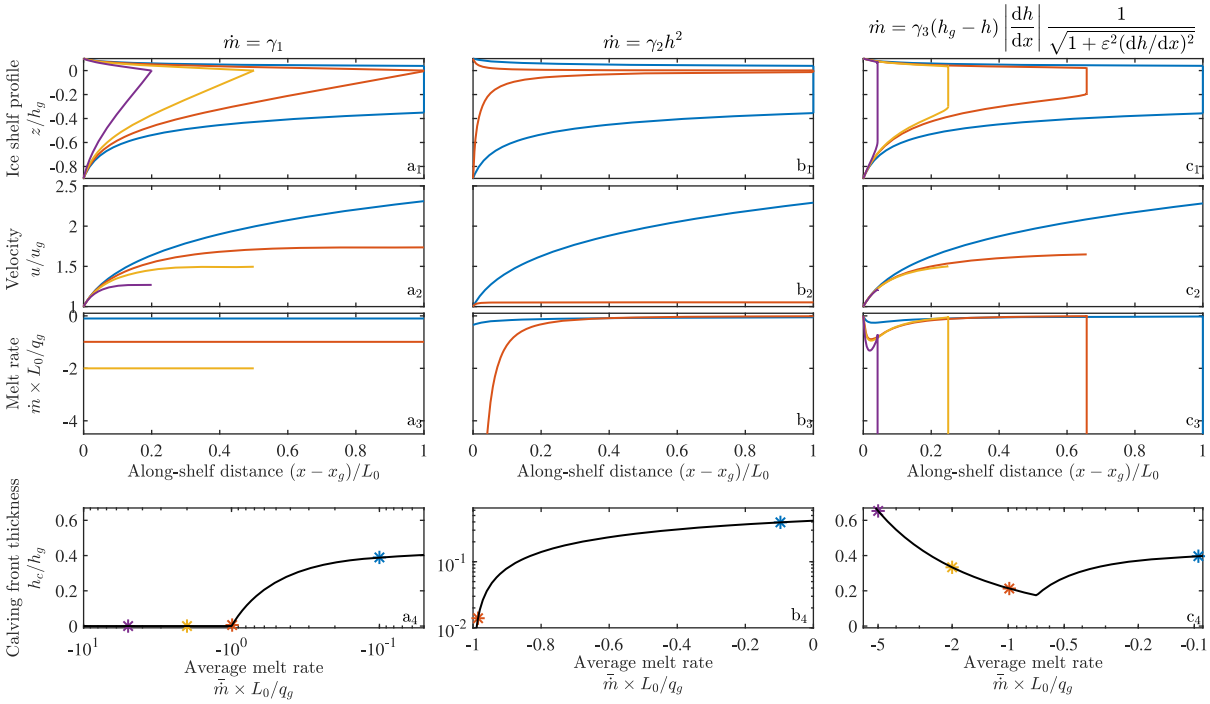

Fig. 2. Examples for unconfined ice-shelf profiles (row 1) and velocities (row 2) for different melt rate distributions (row 3). Profiles in the same colour have the same average melt rates $\bar{\dot{m}} = L_s^{-1}\int_{x_g}^{x_g+L_s} \dot{m}\, dx$ as indicated in panels a_4–c_4. Note that the y-axis of panel b_4 is logarithmic, as the ice thickness remains non-zero for all $\gamma_2 \leq 0$.

steady state. We will see in Section 4.2 that this effect is even more pronounced for buttressed ice shelves experiencing melt.

4. Buttressed marine ice sheets

4.1. The role of the calving law

Before considering the effect of different melt rate parameterizations on grounding-line positions, we focus on the effects of the calving law. We consider steady-state configurations of a 40 km wide marine ice sheet on an overdeepened bed in the absence of submarine melting (Fig. 3). We use the three different calving criteria described in (6), with the calving front position ($x_c \approx 380$ km), ice-shelf length ($L_0 \approx 155$ km), and ice thickness at the calving front ($h_c \approx 416$ m) chosen in such a way that all three calving laws produce the same steady-state configuration on the retrograde part of the bed (panels a_2, b_1 and c_2, respectively). All other parameter values are listed in Table 1.

4.1.1. Steady-state configurations

In steady state, two conditions are simultaneously satisfied at the grounding line: the ice flux matches the accumulation integrated over the grounded part of the ice sheet (10), and the ice thickness is at floatation (9b). To determine grounding-line positions analytically, we use the asymptotic solutions of Θ for constant melt rates derived in Haseloff and Sergienko (2018):

$$\Theta = 1 - \frac{1}{h_g^2}\left(\frac{q_g}{\left[\rho_i g(1-\rho_i/\rho_w)\right]^n A W}\right)^{2/(n+1)} \times \left[(4^n C_w)^{1/(n+1)} + \frac{1+n}{n} C_w \frac{L_s}{W}\right]^{2n/(n+1)}. \tag{18}$$

For a fixed ice thickness at the calving front $(6)_3$, we additionally need a relation between the ice thickness at the calving front and the ice-shelf length, which we approximate with (Haseloff and Sergienko, 2018)

$$h_c = \left[h_{c,unconf}^{(n+1)^2/n}\, \mathrm{erfc}\left(\frac{C_w}{2}\frac{L_s^{1+1/n}}{W^{1+1/n}}\right) + h_{c,conf}^{(n+1)^2/n}\, \mathrm{erf}\left(\frac{C_w}{2}\frac{L_s^{1+1/n}}{W^{1+1/n}}\right)\right]^{n/(n+1)^2}. \tag{19a}$$

$h_{c,unconf}$ is the ice thickness at the calving front of unconfined ice shelves

$$h_{c,unconf} = \frac{2^{2n/(n+1)} h_g q_g^{1/(n+1)}}{\left[2^{2n} q_g + (n+1)[\rho_i g(1-\rho_i/\rho_w)]^n h_g^{1+n} A L_s\right]^{1/(n+1)}} \tag{19b}$$

and $h_{c,conf}$ is the ice thickness at the calving front of strongly buttressed ice shelves

$$h_{c,conf} = \left[\frac{4^n C_w q_g^{1/n+1}}{\left[\rho_i g(1-\rho_i/\rho_w)\right]^{1+n} A^{1/n+1} W^{1/n+1}}\right]^{n/(n+1)^2}. \tag{19c}$$

For illustrative purposes, we solve (8)–(9) numerically with Matlab ODE solvers to obtain the ice-sheet profiles, and (1b) and $(3)_2$ with (10) and (4c) to obtain the ice-shelf profiles.

In our example, the grounding-line flux obtained with a fixed ice-shelf length mirrors the shape of the bed and the analytical and semi-analytical solutions predict three possible steady states (Fig. $3a_1$–a_3), two on the downwards sloping sections of the bed, and one on the upwards sloping part of the bed. Conversely, for a fixed calving front position $x_c = \text{const.}$, we find only one steady-state grounding-line position, located on the retrograde section of the bed (Fig. $3b_1$), as the flux appears to be monotonically increasing over the entire domain (Fig. $3b_4$). Finally, for a fixed ice thickness at the calving front, the ice flux

https://doi.org/10.1017/jog.2022.29 Published online by Cambridge University Press

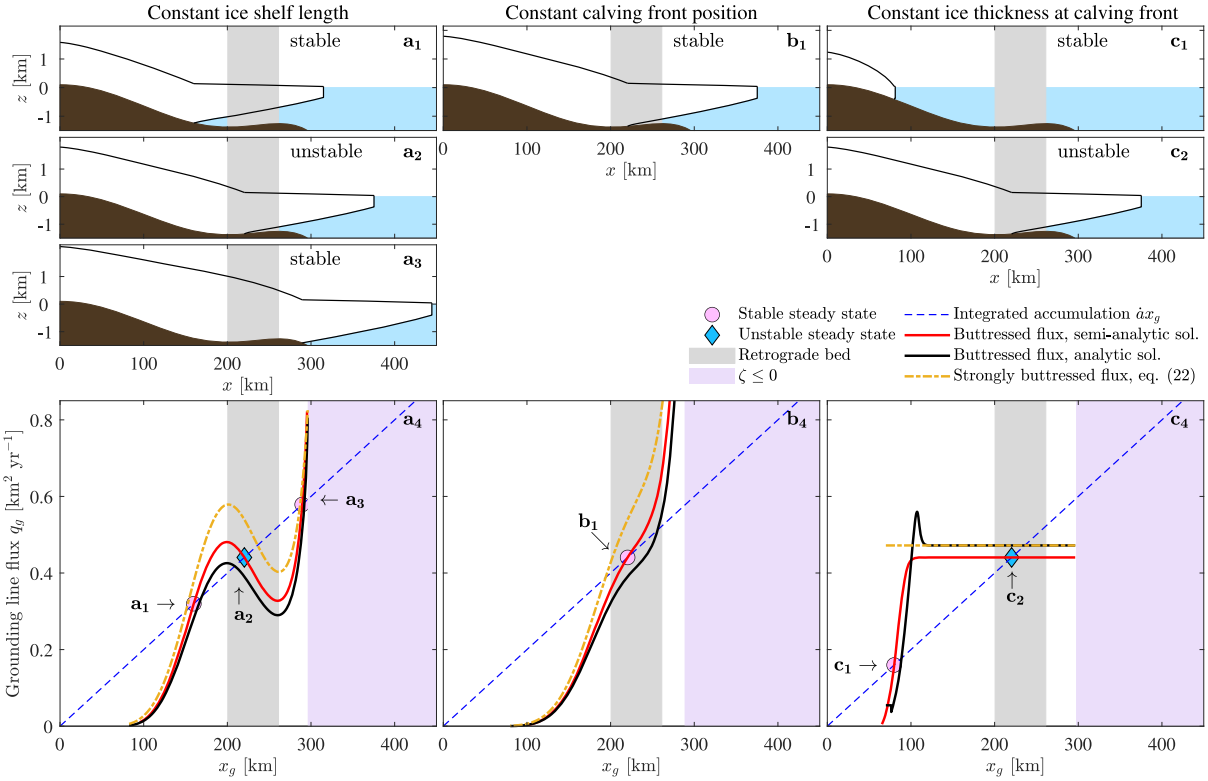

Fig. 3. Extent and stability of a 40 km wide outlet glacier on a bed given by (2) and constant accumulation on the grounded ice sheet. Column a: results for fixed ice-shelf length of 155 km; column b: results for fixed calving front position at $x_c = 380$ km, column c: results for fixed ice thickness $h_c = 415$ m at the calving front. Panels a_4–c_4 show the solutions for the buttressed ice flux q_g at the grounding line and the integrated accumulation (dashed line). At the intersection of the flux q_g with the integrated accumulation steady-state grounding-line positions are possible, which are shown in panels a_1–a_3, b_1, and c_1–c_2.

Table 1. Model parameters with their value, where applicable

Description	Variable	Value	Units
Rate factor	A	10^{-24}	Pa^{-3} s^{-1}
Accumulation rate	$\dot{a}$	2	m a^{-1}
Basal shear stress parameter	C	7.624×10^6	Pa m$^{-1/3}$ s$^{1/3}$
Lateral shear stress parameter	C_w	$2(n+1)^{1/n}$	
Gravity constant	g	9.8	m s^{-2}
Melt rate parameter	γ_1, γ_2, γ_3,		
Ice-shelf length	L_s		m
Sliding parameter	m	1/3	
Submarine melt rate	$\dot{m}$		m a^{-1}
Flow law exponent	n	3	
Density of ice	ρ_i	900	kg m^{-3}
Density of water	ρ_w	1000	kg m^{-3}
Ice-shelf width	W	40×10^3	m

at the grounding line appears independent of the bed shape over most of the domain, with the upstream branch of the flux closely following the shape of the unbuttressed flux (not shown), and the downstream branch of the ice flux being constant. This leads to the existence of two equilibrium grounding-line positions (Fig. 3c_1–c_2), one close to the unbuttressed grounding-line solution with a very short ice shelf (Fig. 3c_1) and one on the retrograde part of the bed (Fig. 3c_2). Note that the analytical flux for a constant thickness at the calving front peaks at $x \approx 100$ km. This is due to the approximation of the calving-front ice thickness with (19a), which is an ad-hoc approximation of the ice thickness at the calving front and only formally correct in the two limits of no and strong buttressing (see Haseloff and Sergienko, 2018).

For all three calving laws, we do not compute the flux at the grounding line q_g past $x \gtrapprox 300$ km. As mentioned above, the slope of the bed db/dx has a large magnitude there, resulting in the bracketed term in the denominator of (13) being negative; such steep bedrock slopes also violate the assumptions of the shallow shelf approximation, which our model is based on (MacAyeal, 1989).

To provide more than one or two points of comparison per calving law, we compare the semi-analytical and analytical results with numerical results for a range of different widths in the appendix (see Fig. 7); there we generally find good agreement between semi-analytical solutions and the numerical solutions.

4.1.2. Stability of steady states

To determine the stability of these steady states, we perform a linear stability analysis described in Appendix C. It shows that the stability of these steady states cannot be determined from comparison of the flux gradient with the accumulation rate alone. Instead, the stability condition depends on the chosen calving law, melt rate parameterization (if we additionally take melting into account) and strength of the bed slope.

In the absence of melting, and assuming that the calving law can be expressed through a calving front position $x_c(x_g, h_g, q_g)$ which is a function of grounding-line position x_g, ice thickness at the grounding line h_g, and ice flux at the grounding line q_g, the general stability condition (C20) can be written in terms of the flux gradient dq_g/dx_g and the accumulation rate $\dot{a}$ (see (C26))

$$\text{if } \left(A_1 + B\frac{q_g^{1/n-1}}{n}\left((4^n C_w)^{1/(n+1)} W + C_w(x_c - x_g)\right) + BC_w q_g^{1/n}\frac{\partial x_c}{\partial q_g}\right) > 0,\ \zeta > 0,\ \left(h_x - \frac{dh_g}{dx_g}\right) < 0$$
$$\text{then for } \begin{cases} \dot{a} < \dfrac{dq_g}{dx_g} & \text{stable} \\ \dot{a} > \dfrac{dq_g}{dx_g} & \text{unstable.} \end{cases} \tag{20}$$

https://doi.org/10.1017/jog.2022.29 Published online by Cambridge University Press

We point out that the flux gradient depends not only on the bed slope (through $\mathrm{d}h_\mathrm{g}/\mathrm{d}x_\mathrm{g}$), but also on the accumulation gradient ($\mathrm{d}\dot{a}/\mathrm{d}x_\mathrm{g}$), bed curvature ($\mathrm{d}^2b/\mathrm{d}x_\mathrm{g}^2$) and buttressing; it is (C23)

$$\frac{\mathrm{d}q_\mathrm{g}}{\mathrm{d}x_\mathrm{g}}=\frac{(B_1-A_2-BC_\mathrm{w}q_\mathrm{g}^{1/n}\frac{\partial x_\mathrm{c}}{\partial h_\mathrm{g}})\frac{\mathrm{d}h_\mathrm{g}}{\mathrm{d}x_\mathrm{g}}-A_3\frac{\mathrm{d}\dot{a}}{\mathrm{d}x_\mathrm{g}}-A_4\frac{\mathrm{d}^2b}{\mathrm{d}x_\mathrm{g}^2}+BC_\mathrm{w}q_\mathrm{g}^{1/n}\left(1-\frac{\partial x_\mathrm{c}}{\partial x_\mathrm{g}}\right)}{A_1+q_\mathrm{g}^{1/n-1}B\left[\frac{1}{n}(4^nC_\mathrm{w})^{1/(n+1)}W+\frac{1}{n}C_\mathrm{w}(x_\mathrm{c}-x_\mathrm{g})+q_\mathrm{g}\frac{\partial x_\mathrm{c}}{\partial q_\mathrm{g}}\right]}. \tag{21}$$

The parameters A_1–A_4 are defined in (C12), the parameters B and B_1 are defined in (C14) and ζ is given by (C11).

This condition is significantly more complex than the stability conditions derived in Schoof (2012) and Sergienko and Wingham (2022), as it takes into account not only accumulation and bed gradients, but also the lateral confinement of the grounded ice sheet and buttressing by the ice shelf. The requirement $A_1+B\frac{q_\mathrm{g}^{1/n-1}}{n}((4^nC_\mathrm{w})^{1/(n+1)}W+C_\mathrm{w}(x_\mathrm{c}-x_\mathrm{g}))+BC_\mathrm{w}q_\mathrm{g}^{1/n}\partial x_\mathrm{c}/\partial q_\mathrm{g}>0$ is a necessary condition to make statements about stability with a linear stability analysis, i.e. without using a full numerical model. $\zeta>0$ is required for steady states to exist; otherwise the denominator in (13) is complex. The condition $h_x-\mathrm{d}h_\mathrm{g}/\mathrm{d}x_\mathrm{g}$ is the requirement that the ice upstream of the grounding line remains grounded (Schoof, 2012). Provided these conditions are satisfied, the difference between the accumulation rate and the flux gradient can indeed be used to determine the stability of a steady state, in the same manner as in the case of Schoof's flux formula (Schoof, 2007b, 2012).

The terms $B\frac{q_\mathrm{g}^{1/n-1}}{n}((4^nC_\mathrm{w})^{1/(n+1)}W+C_\mathrm{w}(x_\mathrm{c}-x_\mathrm{g}))$ and $BC_\mathrm{w}q_\mathrm{g}^{1/n}$ are positive by definition, and we have explicitly chosen our geometry to ensure $A_1>0$. For a constant calving front position ($x_\mathrm{c}=$ constant) or a constant ice-shelf length ($x_\mathrm{c}=x_\mathrm{g}+L_\mathrm{s}$, $L_\mathrm{s}=$ constant), the partial derivative $\partial x_\mathrm{c}/\partial q_\mathrm{g}$ vanishes, and we can use a visible comparison between the flux and integrated accumulation to determine the stability of steady states in Figures 3a, b. For the solutions with a constant ice-shelf length, we can identify the two steady states on the prograde bed (a_1 and a_3) as stable grounding-line positions, while the steady-state grounding-line position on the retrograde part of the bed (a_2) is unstable. However, if the same steady state is obtained with a fixed calving front position, then the steady-state position on the retrograde bed (b_1) becomes stable. The position and stability of these steady states is also confirmed by numerical calculations, see Appendix A.

The flux gradient can be determined from (21), but this expression is complex and does not allow for a straightforward identification of the leading-order processes. To understand the role of the calving law better, we therefore use the limit of strong buttressing (formally when $L_\mathrm{s}\gg W$) to obtain a simplified analytic expression for the grounding-line flux from setting $\Theta=0$ in (18) (see Haseloff and Sergienko, 2018, for details):

$$q_{\mathrm{g},L_\mathrm{s}}=\frac{[\rho_\mathrm{i}g(1-\rho_\mathrm{i}/\rho_\mathrm{w})]^nAW^{n+1}}{(4^nC_\mathrm{w})^{1/(n+1)}W+\frac{1+n}{n}C_\mathrm{w}L_\mathrm{s}}h_\mathrm{g}^{n+1} \quad \text{if } L_\mathrm{s}=\text{const.},\ W\ll L_\mathrm{s}. \tag{22a}$$

Equation (22a) is plotted as a dashed yellow line in Figures 3a$_4$. As it qualitatively agrees with the other solutions, we can use (22a) to better understand the behaviour shown in Figure 3a$_1$–a$_3$: (22a) predicts that all spatial variability in the ice flux is due to changes in the ice thickness at the grounding line $h_\mathrm{g}=-\rho_\mathrm{w}/\rho_\mathrm{i}\,b(x_\mathrm{g})$. This is qualitative similar to the ice-flux expression for unconfined ice sheets by Schoof (2007b) (14), and therefore explains why this calving law reproduces the instability of grounding lines on upwards sloping beds: $\mathrm{d}q_{\mathrm{g},L_\mathrm{s}}/\mathrm{d}x_\mathrm{g}$ is negative for all areas where the bed slopes upwards ($\mathrm{d}b/\mathrm{d}x_\mathrm{g}>0$), so that the grounding line is always unstable on retrograde beds for a constant, positive accumulation rate $\dot{a}$.

For a constant calving front position, the general stability condition (20) predicts that the sole steady state on the retrograde section of the bed is stable. The stability of this grounding line is also confirmed by the numerical solutions in Appendix A. As for the constant ice-shelf length, an explicit flux expression can be obtained in the limit of strong buttressing:

$$q_{\mathrm{g},x_\mathrm{c}}=\frac{[\rho_\mathrm{i}g(1-\rho_\mathrm{i}/\rho_\mathrm{w})]^nAW^{n+1}}{(4^nC_\mathrm{w})^{1/(n+1)}W+\frac{1+n}{n}C_\mathrm{w}(x_\mathrm{c}-x_\mathrm{g})}h_\mathrm{g}^{n+1} \quad \text{if } x_\mathrm{c}=\text{const.},\ W\ll L_\mathrm{s}. \tag{22b}$$

Now, even as the depth of the seafloor decreases with increasing x_g ($\mathrm{d}b/\mathrm{d}x_\mathrm{g}>0$) on upwards sloping parts of the bed, it is possible for the flux to increase due to the second term in the denominator, which decreases with increasing x_g. Physically, this corresponds to the fact that the length of the ice shelf and hence the amount of buttressing decreases as the grounding line advances. Less buttressing leads to an increase in the ice flux, and this increase in ice flux can exceed the reduction in ice flux due to a smaller ice thickness at the grounding line, as shown in Figure 3b$_4$.

When the ice thickness at the calving front is prescribed, Figure 3 shows that we have two branches, the upstream branch where the ice thickness at the calving front is set by (19b) and one where it is set by (19c). For the upstream branch, we can use (19b) to determine $\partial x_\mathrm{c}/\partial q_\mathrm{g}$ as

$$\frac{\partial x_\mathrm{c}}{\partial q_\mathrm{g}}=\frac{4^n\left[1-(h_\mathrm{c}/h_\mathrm{g})^{n+1}\right]}{(n+1)[\rho_\mathrm{i}g(1-\rho_\mathrm{i}/\rho_\mathrm{w})]h_\mathrm{g}^{n+1}A}>0 \quad \text{if } h_\mathrm{c}=h_{\mathrm{c,unconf.}}$$

ensuring $A_1+B\frac{q_\mathrm{g}^{1/n-1}}{n}((4^nC_\mathrm{w})^{1/(n+1)}W+C_\mathrm{w}(x_\mathrm{c}-x_\mathrm{g}))+BC_\mathrm{w}q_\mathrm{g}^{1/n}\frac{\partial x_\mathrm{c}}{\partial q_\mathrm{g}}>0$). Consequently, we can determine from equation (20) that these configurations are stable.

The stability condition (20) does not extend to the case where the ice thickness at the calving front is set by (19c), as this ice thickness directly sets the flux at the grounding line (which one can obtain from rearranging (19c)):

$$q_{\mathrm{g},h_\mathrm{c}}=\frac{[\rho_\mathrm{i}g(1-\rho_\mathrm{i}/\rho_\mathrm{w})]^n}{(4^nC_\mathrm{w})^{n/(n+1)}}AWh_\mathrm{c}^{n+1}. \tag{22c}$$

For a simplified flux condition of this form the Sturm–Liouville problem considered in Appendix C reduces to the regular Sturm–Liouville problem considered in Schoof (2012), and his stability conditions remain valid. As $\mathrm{d}q_{\mathrm{g},h_\mathrm{c}}/\mathrm{d}x_\mathrm{g}=0$, this branch is always unstable for positive accumulation rates.

These examples illustrate that different calving laws produce very different grounding-line positions for buttressed marine ice sheets and that the choice of calving law can change the stability of the grounding line from stable to unstable and vice versa. This suggests that the grounding-line response of buttressed marine ice sheets to different melt forcings will depend on the calving law as well.

4.2. The role of the melt location

We have seen in Section 3 that different melt distributions result in very distinct ice-shelf profiles. In this section and the next, we aim to understand the response of *buttressed* ice sheets to different melt parameterizations. Numerical studies (e.g.,

https://doi.org/10.1017/jog.2022.29 Published online by Cambridge University Press

Gagliardini and others, 2010) suggest that melting closer to the grounding-line affects the grounding-line response more than melting further away from it. We can understand this behaviour by determining the steady-state grounding-line stress for a spatially variable melt rate $\dot{m} = f(x)$ (see Appendix B.2):

$$\frac{\tau_{\text{shelf}}}{\tau_0} = \Theta = 1 - \left[\frac{(4^n C_w)^{1/(1+n)} [q(x_c)]^{1/n} + \frac{n+1 C_w}{n \; W} \int_{x_g}^{x_c} [q(x')]^{1/n} \mathrm{d}x'}{\rho_i g (1-\rho_i/\rho_w) A^{1/n} W^{1/n} h_g^{1/n+1}} \right]^{2n/(n+1)}. \tag{23a}$$

τ_0 is the grounding-line stress of an unconfined ice shelf, given by $(11c)_3$, and $q(x)$ is the steady-state flux on the ice shelf:

$$q(x) = q_g + \int_{x_g}^{x} f(x')\, \mathrm{d}x'. \tag{23b}$$

Equation (23a) shows that the steady-state grounding-line stress depends on the integrated ice flux and the calving flux, that is, the ice flux at the ice-shelf front. Both of these quantities decrease with increasing melt, albeit in different ways. The calving flux is insensitive to the location of melting, and only depends on the total amount of melting experienced throughout the ice shelf, $q(x_c) = q_g + \int_{x_g}^{x_c} f(x')\, \mathrm{d}x'$ with the second term the integrated melt rate on the ice shelf. Conversely, the integrated flux depends on the melt location: the integral $\int_{x_g}^{x_c} q^{1/n}\, \mathrm{d}x$ is smaller if q is reduced closer to x_g for the same amount of reduction. A consequence of (23a) is therefore that melting closer to the grounding line reduces the backstress more than the same amount of melting farther away from the grounding line.

To illustrate the effect of the melt location on the grounding-line position, we consider a δ-function melt perturbation:

$$\dot{m} = -\mu q_g \times \delta(x_m - x), \quad 0 < \mu < 1, \quad x_g < x_m < x_g + L_s \tag{24}$$

i.e. we melt only at a single point on the ice shelf and remove a fraction μ of the grounding-line flux there (note that $\delta(x - x_m)$ has units m^{-1}). We start our calculations from the stable steady state shown in Figure $3a_1$ and keep the ice shelf length constant ($L_0 = 155$ km) to avoid the non-linear effects introduced through more complicated calving laws (Section 4.1).

Figures 4a, b show steady-state profiles for $\mu = 0.5$ and different relative melt locations

$$x_r = (x_m - x_g)/L_0,$$

that is, for different locations of melting relative to the total ice-shelf length; at the grounding line $x_r = 0$. Clearly, in this example moving the location of melting closer to the grounding line leads to steady-state grounding-line positions further inland. Note also the pronounced drop in ice-shelf velocities right downstream of the melt perturbation.

For this example, the stress (23a) with melt rate (24) can be written as a function of relative melt-rate position x_r:

$$\Theta = 1 - \frac{q_g^{2/(n+1)}}{h_g^2} \times \left[\frac{(4^n C_w)^{1/(n+1)} (1-\mu)^{1/n} + \frac{1+n}{n} C_w \frac{L_s}{W} [x_r + (1-\mu)^{1/n}(1-x_r)]}{\rho_i g (1-\rho_i/\rho_w) A^{1/n} W^{1/n}} \right]^{2n/(n+1)}. \tag{25}$$

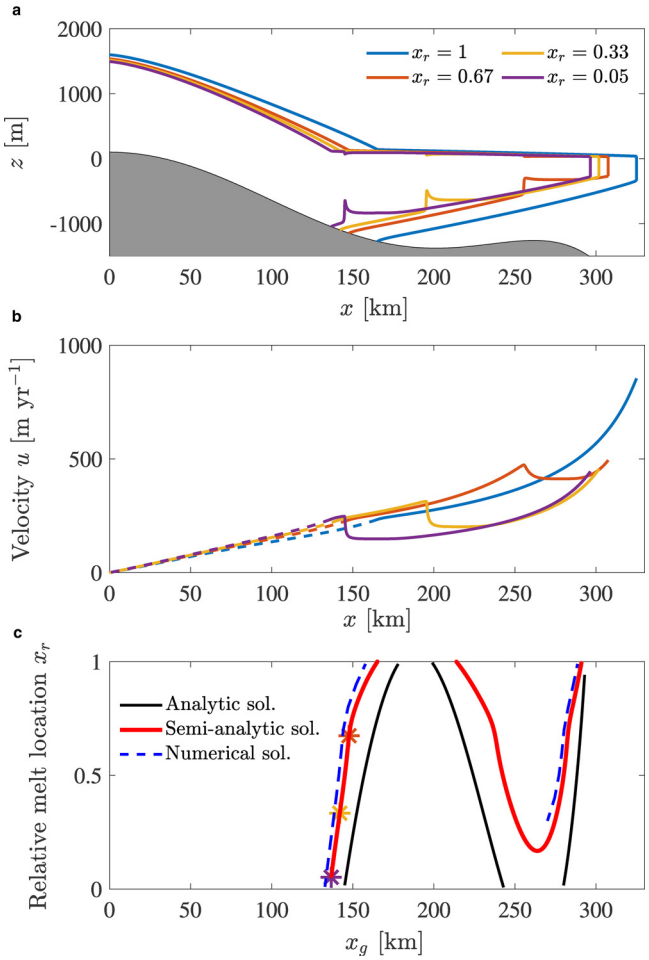

Fig. 4. Influence of relative melt location $x_r = (x_m - x_g)/L_0$ on grounding-line position. $x_r = 0$ corresponds to melting at the grounding line, $x_r = 1$ for melting at the calving front. Panels show ice-sheet/shelf profiles (a), velocities (b) and grounding-line positions (c) for melt applied at different relative melt positions x_r (24). Note that melting closer to the grounding line leads to more grounding-line retreat than melting further farther away from it. Analytic solution obtained with (25).

with $(1-\mu)$ the fraction of the grounding-line ice flux *not* removed by melt. For constant μ, Eqn (25) describes the reduction in buttressing as a monotonically increasing function of the relative melt location x_r, with the change in τ_{shelf} being largest for melting directly at the grounding line ($x_r = 0$) and reducing towards the ice-shelf front ($x_r = 1$). Equation (25) together with (14) provides an analytic (albeit implicit) expression of the grounding-line flux, and these solutions are shown as black lines in Figure 4, together with semi-analytical (red lines) and numerical solutions (dashed blue lines).

While this example of strong localized melting is instructive in understanding some of the factors controlling grounding-line position, it is hardly realistic. We will therefore turn to more realistic (but still highly idealized) melt rates next.

4.3. Combination of melt rate and calving parameterizations

In this section, we explore how steady-state grounding-line positions depend on different combinations of the calving laws considered in Section 4.1 and the melt parameterizations considered in Section 3. We use the same parameters that we used for the examples shown in Figure 3 (listed in Table 1) and the different melt parameterizations introduced in Eqn (5). To calculate grounding-line positions, we use the semi-analytical method described above, which we have shown in Section 4.2 and Appendix A to agree well with the numerical solutions.

https://doi.org/10.1017/jog.2022.29 Published online by Cambridge University Press

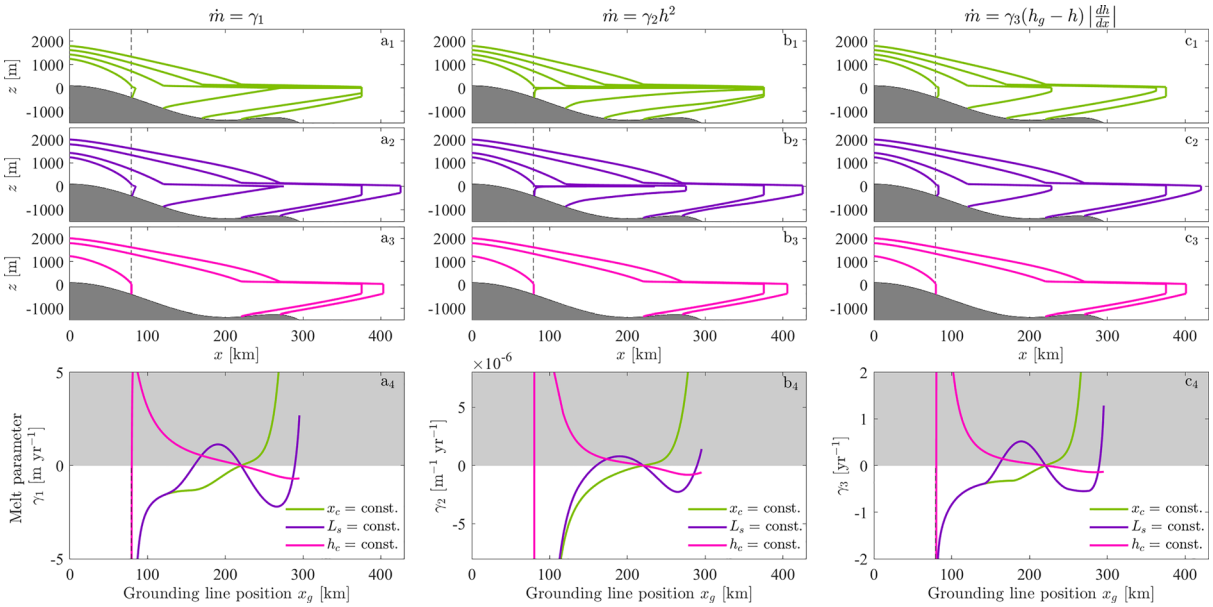

Fig. 5. Steady-state solutions for three different calving laws (indicated by colour) and three different sub-shelf melt parameterizations (indicated by column titles). Ice-sheet/shelf profiles (panels a_1–c_3) are shown in 50 km intervals, but only for negative values of γ_i, as the melt rate parameterizations are not applicable for freeze-on. Values of the melt rate parameters γ_i at corresponding steady-state grounding-line positions shown in panels a_4–c_4. Note that γ_i has different units for different melt rate parameterizations, therefore numerical values are not directly comparable between different parameterizations. For all melt rates more negative values correspond to more melting.

For all combinations, we start with the same melt-free configurations shown in Figure 3 ($\gamma_1 = \gamma_2 = \gamma_3 = 0$). We then vary the melt rate parameters γ_1, γ_2 or γ_3, respectively, while keeping either the calving front position fixed (green lines in Fig. 5), the ice-shelf length fixed (purple lines) or the ice thickness at the calving front fixed (magenta lines). Columns a–c in Figure 5 correspond to the different melt rate parameterizations considered, and the first three panels show the corresponding steady-state ice-sheet/shelf profiles for each calving law. For completeness, we also include solutions for positive values of γ_i in panels a_4–c_4 (but not in the profiles), even though these correspond to freeze-on, and the models are not applicable in this parameter range.

The ice-shelf profiles at one fixed grounding-line position can differ substantially both between different melt rate parameterizations (compare for example panels a_1–c_1) and different calving laws (compare for example panels b_1–b_3). At least the former should not come as a surprise, as this mirrors the behaviour seen in Section 3. There are, however, also some common characteristics. For example the solutions with a fixed ice thickness at the calving front (panels a_3–c_3) are virtually indistinguishable for different melt rate parameterizations. We can also note that the solutions for a fixed ice-shelf length and for a fixed calving front with a constant melt rate are identical in the cases of strong melting when the length of the ice shelf is set by the position where all ice is removed through melting (panels a_1 and a_2). The same is true for the slope-dependent melt rate when the melt rate parameter γ_3 exceeds the critical value γ_c (panels c_1 and c_2).

γ_1, γ_2 and γ_3 represent different physical quantities, therefore they are not directly comparable. Instead, we compare the average ice-shelf melt rate, Figure 6, with the colour indicating the calving law and the line type indicating the melt rate parameterization. Perhaps the most striking property of Figure 6 is that solutions with the same calving law are more similar to each other than solutions with the same melt rate parameterization, and that their shape roughly mirrors the shape of the grounding-line flux in the absence of melt, compare Figures $3a_4$–c_4. Nevertheless, there is a large spread in average melt rates

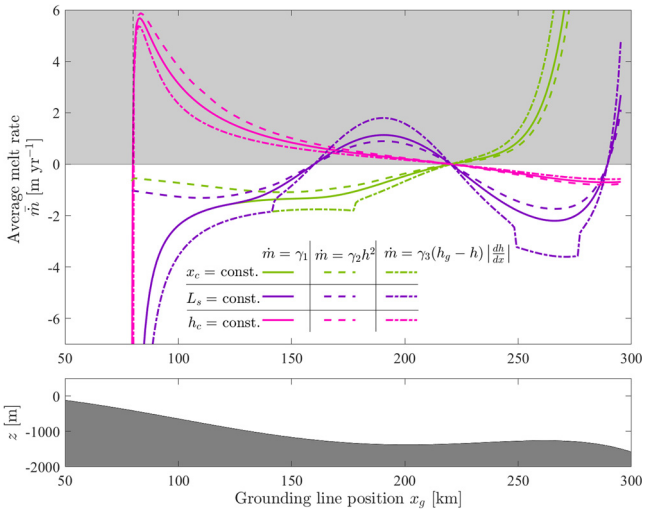

Fig. 6. Average melt rate $\bar{\dot{m}} = L_s^{-1} \int_{x_g}^{x_g + L_s} \dot{m}\, dx$ vs grounding-line position for solutions shown in Figure 5.

associated with different steady-state grounding-line positions. For example, the average melt rate $\bar{\dot{m}}$ associated with a grounding line close to the unbuttressed grounding line at $x \approx 80$ km ranges from $\bar{\dot{m}} \approx -6$ m a^{-1} to $\bar{\dot{m}} \approx -1$ m a^{-1} (ignoring positive values, as these are only included for completeness).

Figure 6 illustrates that the grounding-line positions obtained with the thickness-based calving law (magenta lines) follow qualitatively different relationships between average melt rate and steady-state grounding-line position than the other two calving laws. The grounding-line positions are largely insensitive to the melt distribution and the average melt rates required to change the steady-state grounding-line position are substantially lower than the melt rates required for the other calving laws. This behaviour is linked to the grounding-line flux for this calving law, see Figure 3, which is essentially bi-modal: either mostly following the flux expression for the unbuttressed case, or constant for different grounding-line positions.

https://doi.org/10.1017/jog.2022.29 Published online by Cambridge University Press

The other two calving laws overlap when subjected to the strong melt forcing with constant ($\dot{m} = \gamma_1$, solid green and purple lines) or slope-dependent melting ($\dot{m} = \gamma_3(h_g - h)|dh/dx|$, dash-dotted green and purple lines). This is not surprising, as in these cases the ice-shelf length is set by the location where the ice thickness goes to zero, rather than the calving law (compare profiles in a_1–a_2 and c_1–c_2, respectively).

The average melt rate associated with a particular steady-state grounding-line position is usually the highest for the plume-like parameterization, as it predicts strong frontal melting for large values of γ_3. Our results in 4.2 showed that melting at the ice-shelf front has less impact on the backstress at the grounding line, even though it leads to high average melt rates. Conversely, the average melt rates obtained with the thickness-based parameterization $\dot{m} = \gamma_2 h^2$ are lower than for the other melt rates, as in this case melting is strongest at the grounding line, where it has maximum impact because of the integral dependence of the buttressing parameter on melting.

For a constant melt rate $\dot{m} = \gamma_1$, we can use the results of the linear stability analysis in Appendix C to determine the stability of the steady states shown here, which generally reproduces the same stability behaviour that we have seen in Section 4.1. However, these results cannot be extended to the other two parameterizations, as the stability condition (C20) is specific to the flux parameterization (13) with (23a), the solution for Θ for $\dot{m} = f(x)$. If the expressions for Θ were known for the other two melt rate parameterizations, it would be possible to extend the stability analysis using the same methodology as presented in Appendix C.

5. Discussion

In this study, we have considered how different ice-shelf mass-loss processes affect the steady-state configurations and stability of confined marine ice sheets. To this end, we have derived an expression for the ice flux at the grounding line, which extends the results of earlier studies by Schoof (2007b), Haseloff and Sergienko (2018) and Sergienko and Wingham (2022), and accounts for the lateral confinement of the grounded ice sheet and ice-shelf buttressing. Using this expression, we have compared steady-state grounding-line positions obtained with different melt rate and calving parameterizations. By means of a linear stability analysis, we have derived stability conditions for a specific form of the buttressing parameter Θ.

5.1. The role of calving

Our results suggest that the variability in grounding-line positions due to different calving laws is greater than the variability due to different melt rate parameterizations. We find that using different calving parameterizations can change the response of grounding lines to forcing qualitatively – from a stable to an unstable configuration. In contrast, using different melt parameterizations only changed this response quantitatively by changing the average melt rate associated with a particular grounding-line position.

This difference is due to the different ways these parameterizations are formulated: the calving laws we introduced change the length of the ice shelf as a function of grounding-line position (due to their dependencies on x_g, h_g and q_g), compare for example the simplified flux expressions (22a)–(22c). In contrast, the melt parameterizations differ in their spatial distribution of melt rates, but do not alter the length of the ice shelf for most of the parameters we considered. Only when melting becomes strong enough to determine the ice-shelf length, do the differences between different calving laws vanish (e.g. see the grounding-line positions for x_c = const. and L_s = const. in the limit of strong melting, Figs 5a_4, c_4).

The grounding-line flux depends on the specifics of the calving law and melt parameterization, therefore a generalized stability criterion cannot be derived. Instead, stability conditions have to be evaluated on a case-by-case basis for specific formulations. Our linear stability analysis provides a template for this process and gives a stability criterion for melt rates of the form $\dot{m} = f(x)$. Provided the bed is sufficiently smooth and the steady-state calving front position does not retreat with increasing grounding-line flux, the stability condition can be formulated in terms of the gradient of the grounding-line flux dq_g/dx_g and the accumulation rate, in line with Schoof (2012). Application of these results illustrates that stable grounding-line positions on upwards sloping beds obtained with a constant calving front position are indeed due to the increase of ice-shelf length and hence buttressing with grounding-line retreat (as suggested by Schoof and others, 2017).

However, linear stability analyses that can provide stability conditions are only possible if the flux expression is explicitly known. Even the simple melt rate parameterizations considered here do not always provide a closed-form expression of the backstress at the grounding line. Therefore generalized inferences about the (in)stability of one particular glacier are impossible without detailed numerical studies.

5.2. The role of melting

We find that the buttressed grounding-line flux depends at leading order on the integrated ice-shelf flux or the double integral of the melt-rate distribution (Eqn (23)). Numerical studies suggest that melting closer to the grounding-line affects grounding-line dynamics more than melting away from it (e.g. Gagliardini and others, 2010), and our results provide an analytical confirmation and explanation of these numerical results: the closer to the grounding-line melting occurs, the stronger is the reduction in the integrated ice-shelf flux.

We explore the effects of using different melt parameterizations, which can lead to a large spread in ice-shelf profiles and grounding-line positions for the same average melt rate. In particular, one of the melt parameterizations we considered includes a positive feedback between melting and ice-shelf slope (see $(5)_3$), whereas increased melting leads to steeper slopes of the ice-shelf base, which in turn increases melting there. In our model this positive feedback leads to a threshold γ_c of the melt rate parameter γ_3, which regulates the strength of melting. If $\gamma_3 < \gamma_c$ the above feedback leads to singular melt rates at the ice-shelf front, akin to strong frontal melting. This gives the appearance of the ice only thinning up to an *apparent* minimum ice-shelf thickness at the ice-shelf front; past this minimum thickness, further melting appears to lead to ice-shelf retreat, rather than further thinning. We emphasize that this is only an apparent minimum ice-shelf thickness, as the ice thickness in fact goes to zero over a short boundary layer whose extent depends on a regularization parameter.

The existence of this positive feedback has been recognized by other authors (e.g. Jenkins, 1991; Little and others, 2012; Sergienko and others, 2013; Slater and others, 2017). The main difference between our study and these authors is the direct coupling with an ice-sheet/shelf flow model. The coupling with the ice-shelf flow model is essential for the feedback to operate fully, as both ice thickness and flow change in response to melting (see also Sergienko and others, 2013). The latter point is best illustrated by our results for strong localized melting (Section 4.2), which illustrates that the response to melting is not only thinning. In some of our examples the velocity response to melting is much

https://doi.org/10.1017/jog.2022.29 Published online by Cambridge University Press

more pronounced than the ice thickness response. This is because for the steady states considered here, melting reduces the ice flux, which is the product of ice thickness and velocity, and it is not immediately obvious which of these will show a larger response. In other words, without modelling ice-shelf flow and its mass balance simultaneously, one might expect the ice shelf to simply thin in response to melting, but clearly this is not always the case. This also reiterates that one might expect very different long-term and short-term responses to melting, and that further studies of this time-dependent behaviour are necessary to understand these dynamics.

Another difference to these earlier studies is that they use the full plume model, which means the singularity in $(5)_3$, which we regularized through inclusion of an artificial regularization parameter ϵ, is removed and the positive feedback is automatically bounded. Nevertheless, the existence of this positive feedback poses questions about the importance melting plays in settings which allow for the formation of strong submarine plumes. If strong melting leads to severe undercutting, then this could trigger calving of the undercut ice-shelf parts. This could appear as ice-thickness or stress-threshold calving similar to observed calving behaviour of Columbia Glacier, Alaska, USA (Van der Veen, 1996). That said, observations and modelling studies also suggest that the positive feedback might be limited by other factors, for instance, the inclusion of lateral variations in melt (e.g. Gladish and others, 2012; Sergienko, 2013; Langley and others, 2014).

5.3. Model limitations

Systematic comparison of different melt parameterizations and calving laws in time-dependent numerical models is challenging, not least because the melt rate parameters used in different parameterizations are not directly comparable and the numerical effort to accurately calculate grounding-line positions remains significant. Our approach allows us to compare nine different combinations of melt rates and calving laws, but the price for this computational efficiency is a simplified model that neglects several important aspects.

We consider steady states only, and therefore cannot make any statements about the transient evolution of buttressed marine ice sheets. There are several timescales to consider for the ice shelf: in a time-dependent model the immediate effect of changing the melt rate is a change in the ice thickness h (as e.g. considered in Reese and others, 2018a; Zhang and others, 2020), rather than the ice flux $\mathbf{q}$ as the depth-integrated mass balance is $\partial h/\partial t + \nabla \cdot \mathbf{q} = \dot{m}$. It is thus conceivable that transient changes in the grounding-line stress differ substantially from the steady-state response. As such, our steady-state results can only give an indication of the direction of change we anticipate. Moreover, in time-dependent models, calving *rates* are often applied, i.e. instead of prescribing the ice-shelf length directly, the rate of change in calving front position $\dot{x}_c$ is prescribed, which introduces an additional timescale. Depending on this timescale, the relative importance of calving and melting processes might change if the timescale associated with calving is long in comparison with the timescale over which the ice-shelf geometry adjusts to melting.

We have strictly focused on geometric settings that allow us to apply the flux parameterizations developed in Schoof (2007a), Haseloff and Sergienko (2018) and Sergienko and Wingham (2022). This requires a constant width. We have also neglected the effects of varying basal boundary conditions. Relaxing any of these assumptions is known to alter the dynamics of buttressed marine ice sheets (Gomez and others, 2010; Robel and others, 2014, 2016; Brondex and others, 2017; Åkesson and others, 2018; Reese and others, 2018b; Sergienko and Wingham, 2019, 2022).

6. Conclusions

Calving and melt parameterizations strongly influence the grounding-line positions obtained for marine ice sheets with laterally confined ice shelves. With everything else held constant, different calving laws result in qualitatively different ice-sheet configurations and stability properties. Conversely, for a given calving parameterization, ice-sheet steady-state configurations and their stability are less sensitive to different melt parameterizations. If the melt rate depends on the ice-shelf slope, melt rates can become singular, leading to an apparent lower limit of the ice thickness at the ice-shelf front. Consequently, model results of marine ice-sheet evolution strongly depend on the way ice-shelf mass loss is parameterized.

Acknowledgements. MH acknowledges financial support through a VC Senior Fellowship at Northumbria University. OS is supported by award NA18OAR4320123 from the National Oceanic and Atmospheric Administration, USDepartment of Commerce. The statements, findings, conclusions and recommendations are those of the authors and do not necessarily reflect the views of the National Oceanic and Atmospheric Administration, or the US Department of Commerce. We thank an anonymous reviewer and T. Zhang whose comments helped to improve and clarify the manuscript.

References

Åkesson H, Nisancioglu KH and Nick FM (2018) Impact of fjord geometry on grounding line stability. *Frontiers in Earth Science* **6**, 71. doi: 10.3389/feart.2018.00071

Arthern RJ and Williams CR (2017) The sensitivity of West Antarctica to the submarine melting feedback. *Geophysical Research Letters* **44**(5), 2352–2359. doi: FF10.1002/2017GL072514

Aschwanden A, and 7 others (2019) Contribution of the Greenland Ice Sheet to sea level over the next millennium. *Science Advances* **5**(6), eaav9396. doi: 10.1126/sciadv.aav9396

Åström J, and 6 others (2013) A particle based simulation model for glacier dynamics. *The Cryosphere* **7**(5), 1591–1602. doi: 10.5194/tc-7-1591-2013

Bassis JN and Jacobs S (2013) Diverse calving patterns linked to glacier geometry. *Nature Geoscience* **6**, 833–836. doi: 10.1038/ngeo1887

Benn DI, Hulton NRJ and Mottram RH (2007a) 'Calving laws', 'sliding laws' and the stability of tidewater glaciers. *Annals of Glaciology* **46**, 123–130. doi: 10.3189/172756407782871161

Benn DI, Warren CR and Mottram RH (2007b) Calving processes and the dynamics of calving glaciers. *Earth-Science Reviews* **82**, 143–179. doi: 10.1016/j.earscirev.2007.02.002

Brondex J, Gagliardini O, Gillet-Chaulet F and Durand G (2017) Sensitivity of grounding line dynamics to the choice of the friction law. *Journal of Glaciology* **63**(241), 854–866. doi: 10.1017/jog.2017.51

Choi Y, Morlighem M, Rignot E and Wood M (2021) Ice dynamics will remain a primary driver of Greenland ice sheet mass loss over the next century. *Communications Earth & Environment* **2**(1), 1–9. doi: 10.1038/s43247-021-00092-z

Cornford SL, and 10 others (2020) Results of the third Marine Ice Sheet Model Intercomparison Project (MISMIP+). *The Cryosphere* **14**(7), 2283–2301. doi: 10.5194/tc-14-2283-2020

De Rydt J and Gudmundsson GH (2016) Coupled ice shelf–ocean modeling and complex grounding line retreat from a seabed ridge. *Journal of Geophysical Research: Earth Surface* **121**(5), 865–880. doi: 10.1002/2015JF003791

Dupont TK and Alley RB (2005) Assessment of the importance of ice-shelf buttressing to ice-sheet flow. *Geophysical Research Letters* **32**, L04503. doi: 10.1029/2004GL022024

Favier L, and 8 others (2014) Retreat of Pine Island Glacier controlled by marine ice-sheet instability. *Nature Climate Change* **4**(2), 117–121. doi: 10.1038/nclimate2094

Favier L, and 7 others (2019) Assessment of sub-shelf melting parameterisations using the ocean–ice-sheet coupled model NEMO(v3.6)–Elmer/Ice (v8.3). *Geoscientific Model Development* **12**(6), 2255–2283. doi: 10.5194/gmd-12-2255-2019

Fowler AC and Larson DA (1978) On the flow of polythermal glaciers. I. Model and preliminary analysis. *Proceedings of the Royal*

Society of London. Series A, Mathematical and Physical Sciences **363**(1713), 217–242. doi: 10.1098/rspa.1978.0165

Gagliardini O, Durand G, Zwinger T, Hindmarsh RCA and Le Meur E (2010) Coupling of ice-shelf melting and buttressing is a key process in ice-sheets dynamics. *Geophysical Research Letters* **37**(14), L14501. doi: 10.1029/2010GL043334

Gladish CV, Holland DM, Holland PR and Price SF (2012) Ice-shelf basal channels in a coupled ice/ocean model. *Journal of Glaciology* **58**(212), 1227–1244. doi: 10.3189/2012JoG12J003

Goldberg DN, and 5 others (2012) Investigation of land ice–ocean interaction with a fully coupled ice–ocean model: 1. Model description and behavior. *Journal of Geophysical Research: Earth Surface* **117**(F2), F02037. doi: 10.1029/2011JF002246

Goldberg D and 7 others (2018) Representing grounding line migration in synchronous coupling between a marine ice sheet model and a z-coordinate ocean model. *Ocean Modelling* **125**, 45–60. doi: 10.1016/j.ocemod.2018.03.005

Goldberg D, Gourmelen N, Kimura S, Millan R and Snow K (2019) How accurately should we model ice shelf melt rates?. *Geophysical Research Letters* **46**(1), 189–199. doi: 10.1029/2018GL080383

Goldberg D, Holland DM and Schoof C (2009) Grounding line movement and ice shelf buttressing in marine ice sheets. *Journal of Geophysical Research* **114**(F4), F04026. doi: 10.1029/2008JF001227

Gomez N, Mitrovica JX, Huybers P and Clark PU (2010) Sea level as a stabilizing factor for marine-ice-sheet grounding lines. *Nature Geoscience* **3** (12), 850–853. doi: 10.1038/ngeo1012

Gudmundsson GH (2003) Transmission of basal variability to a glacier surface. *Journal of Geophysical Research* **108**, 002107. doi: 10.1029/2002JB002107.

Gudmundsson GH (2013) Ice-shelf buttressing and the stability of marine ice sheets. *The Cryosphere* **7**, 647–655. doi: 10.5194/tc-7-647-2013

Gudmundsson GH, Krug J, Durand G, Favier L and Gagliardini O (2012) The stability of grounding lines on retrograde slopes. *The Cryosphere* **6**, 1497–1505. doi: 10.5194/tc-6-1497-2012

Haseloff M and Sergienko OV (2018) The effect of buttressing on grounding line dynamics. *Journal of Glaciology* **64**(245), 417–431. doi: 10.1017/jog.2018.30

Hewitt IJ (2020) Subglacial plumes. *Annual Review of Fluid Mechanics* **52**, 145–169. doi: 10.1146/annurev-fluid-010719-060252

Hindmarsh RCA (2012) An observationally validated theory of viscous flow dynamics at the ice-shelf calving front. *Journal of Glaciology* **58**(208), 375–387. doi: 10.3189/2012JoG11J206

Holland DM, Thomas RH, De Young B, Ribergaard MH and Lyberth B (2008) Acceleration of Jakobshavn Isbrae triggered by warm subsurface ocean waters. *Nature Geoscience* **1**(10), 659–664. doi: 10.1038/ngeo316

Hughes T (1973) Is the West Antarctic Ice Sheet disintegrating?. *Journal of Geophysical Research* **78**, 7884–7910. doi: 10.1029/JC078i033p07884

Jamieson SSR, and 6 others (2012) Ice-stream stability on a reverse bed slope. *Nature Geoscience* **5**(11), 799–802. doi: 10.1038/ngeo1600

Jenkins A (1991) A one-dimensional model of ice shelf–ocean interaction. *Journal of Geophysical Research: Oceans* **96**(C11), 20671–20677. doi: 10.1029/91JC01842

Jenkins A (2011) Convection-driven melting near the grounding lines of ice shelves and tidewater glaciers. *Journal of Physical Oceanography* **41**(12), 2279–2294. doi: 10.1175/JPO-D-11-03.1

Jordan JR, and 7 others (2018) Ocean-forced ice-shelf thinning in a synchronously coupled ice–ocean model. *Journal of Geophysical Research: Oceans* **123**(2), 864–882. doi: 10.1002/2017JC013251

Joughin I, Smith BE and Holland DM (2010) Sensitivity of 21st century sea level to ocean–induced thinning of Pine Island Glacier, Antarctica. *Geophysical Research Letters* **37**(20), L20502. doi: 10.1029/2010GL044819

Joughin I, Smith BE and Medley B (2014) Marine ice sheet collapse potentially under way for the Thwaites Glacier Basin, West Antarctica. *Science* **344**(6185), 735–738. doi: 10.1126/science.1249055

Langley K, and 8 others (2014) Complex network of channels beneath an Antarctic ice shelf. *Geophysical Research Letters* **41**(4), 1209–1215. doi: 10.1002/2013GL058947

Lazeroms WMJ, Jenkins A, Gudmundsson GH and van de Wal RSW (2018) Modelling present-day basal melt rates for Antarctic ice shelves using a parametrization of buoyant meltwater plumes. *The Cryosphere* **12**(1), 49–70. doi: 10.5194/tc-12-49-2018

Lazeroms WMJ, Jenkins A, Rienstra SW and van de Wal RSW (2019) An analytical derivation of ice-shelf basal melt based on the dynamics of meltwater plumes. *Journal of Physical Oceanography* **49**(4), 917–939. doi: 10.1175/JPO-D-18-0131.1

Levermann A, and 5 others (2012) Kinematic first-order calving law implies potential for abrupt ice-shelf retreat. *The Cryosphere* **6**(2), 273–286. doi: 10.5194/tc-6-273-2012

Little CM, Goldberg D, Gnanadesikan A and Oppenheimer M (2012) On the coupled response to ice-shelf basal melting. *Journal of Glaciology* **58** (208), 203–215. doi: 10.3189/2012JoG11J037

MacAyeal DR (1989) Large-scale ice flow over a viscous basal sediment – theory and application to Ice Stream B, Antarctica. *Journal of Geophysical Research* **94**, 4071–4087. doi: 10.1029/JB094iB04p04071

MacAyeal DR and Barcilon V (1988) Ice-shelf response to ice-stream discharge fluctuations: I. Unconfined ice tongues. *Journal of Glaciology* **34** (116), 121–127. doi: 10.3189/S002214300000914X

Mercer JH (1978) West Antarctic ice sheet and CO_2 greenhouse effect: a threat of disaster. *Nature* **271**, 321–325. doi: 10.1038/271321a0

Morland LW and Johnson IR (1980) Steady motion of ice sheets. *Journal of Glaciology* **25**(92), 229–246. doi: 10.3189/S0022143000010467

Morlighem M, and 6 others (2016) Modeling of Store Gletscher's calving dynamics, West Greenland, in response to ocean thermal forcing. *Geophysical Research Letters* **43**(6), 2659–2666. doi: 10.1002/2016GL067695

Nick F, Van Der Veen C, Vieli A and Benn D (2010) A physically based calving model applied to marine outlet glaciers and implications for the glacier dynamics. *Journal of Glaciology* **56**(199), 781–794. doi: 10.3189/002214310794457344

Nick FM, Vieli A, Howat IM and Joughin I (2009) Large-scale changes in Greenland outlet glacier dynamics triggered at the terminus. *Nature Geoscience* **2**, 110–114. doi: 10.1038/ngeo394

Pegler SS (2016) The dynamics of confined extensional flows. *Journal of Fluid Mechanics* **804**, 24–57. doi: 10.1017/jfm.2016.516

Pegler SS (2018a) Marine ice sheet dynamics: the impacts of ice-shelf buttressing. *Journal of Fluid Mechanics* **857**, 605–647. doi: 10.1017/jfm.2018.741

Pegler SS (2018b) Suppression of marine ice sheet instability. *Journal of Fluid Mechanics* **857**, 648–680. doi: 10.1017/jfm.2018.742

Pegler SS, Kowal KN, Hasenclever LQ and Worster MG (2013) Lateral controls on grounding-line dynamics. *Journal of Fluid Mechanics* **722**, R1. doi: 10.1017/jfm.2013.140

Pegler SS and Worster MG (2012) Dynamics of a viscous layer flowing radially over an inviscid ocean. *Journal of Fluid Mechanics* **696**, 152–174. doi: 10.1017/jfm.2012.21

Pollard D and DeConto RM (2012) Description of a hybrid ice sheet-shelf model, and application to Antarctica. *Geoscientific Model Development* **5** (5), 1273–1295. doi: 10.5194/gmd-5-1273-2012

Pritchard HD, and 5 others (2012) Antarctic ice-sheet loss driven by basal melting of ice shelves. *Nature* **484**(7395), 502–505. doi: 10.1038/nature10968

Reese R, Gudmundsson GH, Levermann A and Winkelmann R (2018a) The far reach of ice-shelf thinning in Antarctica. *Nature Climate Change* **8**(1), 53–57. doi: 10.1038/s41558-017-0020-x

Reese R, Winkelmann R and Gudmundsson GH (2018b) Grounding-line flux formula applied as a flux condition in numerical simulations fails for buttressed Antarctic ice streams. *The Cryosphere* **12**(10), 3229–3242. doi: 10.5194/tc-12-3229-2018

Robel A, Schoof C and Tziperman E (2014) Rapid grounding line migration induced by internal ice stream variability. *Journal of Geophysical Research* **119**(11), 2430–2447. doi: 10.1002/2014JF003251

Robel AA, Schoof C and Tziperman E (2016) Persistence and variability of ice-stream grounding lines on retrograde bed slopes. *The Cryosphere* **10** (4), 1883–1896. doi: 10.5194/tc-10-1883-2016

Robel AA, Seroussi H and Roe GH (2019) Marine ice sheet instability amplifies and skews uncertainty in projections of future sea-level rise. *Proceedings of the National Academy of Sciences* **116**(30), 14887–14892. doi: 10.1073/pnas.1904822116

Rosier SHR, and 5 others (2021) The tipping points and early warning indicators for Pine Island Glacier, West Antarctica. *The Cryosphere* **15**(3), 1501–1516. doi: 10.5194/tc-15-1501-2021

Schoof C (2007a) Ice sheet grounding line dynamics: steady states, stability, and hysteresis. *Journal of Geophysical Research* **112**, F03S28. doi: 10.1029/2006JF000664

Schoof C (2007b) Marine ice-sheet dynamics. Part 1. The case of rapid sliding. *Journal of Fluid Mechanics* **573**, 27–55. doi: 10.1017/S0022112006003570

Schoof C (2011) Marine ice-sheet dynamics. Part 2: A Stokes flow contact problem. *Journal of Fluid Mechanics* **679**, 122–155. doi: 10.1017/jfm.2011.129

Schoof C (2012) Marine ice sheet stability. *Journal of Fluid Mechanics* **698**, 62–72. doi: 10.1017/jfm.2012.43

https://doi.org/10.1017/jog.2022.29 Published online by Cambridge University Press

Schoof C, Davis AD and Popa TV (2017) Boundary layer models for calving marine outlet glaciers. *The Cryosphere* **11**(5), 2283–2303. doi: 10.5194/tc-11-2283-2017

Sergienko OV (2012) The effects of transverse bed topography variations in ice-flow models. *Journal of Geophysical Research: Earth Surface* **117**(F3), F03011. doi: 10.1029/2011JF002203

Sergienko O (2013) Basal channels on ice shelves. *Journal of Geophysical Research: Earth Surface* **118**(3), 1342–1355. doi: 10.1002/jgrf.20105

Sergienko OV (2022) Marine outlet glacier dynamics, steady states and steady-state stability. *Journal of Glaciology*, 1–15. doi: 10.1017/jog.2022.13.

Sergienko OV, Goldberg DN and Little CM (2013) Alternative ice shelf equilibria determined by ocean environment. *Journal of Geophysical Research* **118**(2), 970–981. doi: 10.1002/jgrf.20054

Sergienko O and Wingham D (2019) Grounding line stability in a regime of low driving and basal stresses. *Journal of Glaciology* **65**(253), 833–849. doi: 10.1017/jog.2019.53

Sergienko OV and Wingham DJ (2022) Bed topography and marine ice-sheet stability. *Journal of Glaciology* **68**(267), 124–138. doi: 10.1017/jog.2021.79

Seroussi H, and 6 others (2017) Continued retreat of Thwaites Glacier, West Antarctica, controlled by bed topography and ocean circulation. *Geophysical Research Letters* **44**(12), 6191–6199. doi: 10.1002/2017GL072910

Slater DA, Nienow PW, Goldberg DN, Cowton TR and Sole AJ (2017) A model for tidewater glacier undercutting by submarine melting. *Geophysical Research Letters* **44**(5), 2360–2368. doi: 10.1002/2016GL072374

Straneo F and Heimbach P (2013) North Atlantic warming and the retreat of Greenland's outlet glaciers. *Nature* **504**(7478), 36–43. doi: 10.1038/nature12854

Thomas RH and Bentley CR (1978) A model for Holocene retreat of the West Antarctic Ice Sheet. *Quaternary Research* **10**, 150–170. doi: 10.1016/0033-5894(78)90098-4

Tsai VC, Stewart AL and Thompson AF (2015) Marine ice-sheet profiles and stability under Coulomb basal conditions. *Journal of Glaciology* **61**(226), 205–215. doi: 10.3189/2015JoG14J221

Van der Veen CJ (1996) Tidewater calving. *Journal of Glaciology* **42**(141), 375–385. doi: 10.3189/S0022143000004226

Van der Veen CJ (1998) Fracture mechanics approach to penetration of surface crevasses on glaciers. *Cold Regions Science and Technology* **27**(1), 31–47. doi: 10.1016/S0165-232X(97)00022-0

Vieli A, Funk M and Blatter H (2000) Tidewater glaciers: frontal flow acceleration and basal sliding. *Annals of Glaciology* **31**, 217–221. doi: 10.3189/172756400781820417

Vieli A, Funk M and Blatter H (2001) Flow dynamics of tidewater glaciers: a numerical modelling approach. *Journal of Glaciology* **47**(159), 595–606. doi: 10.3189/172756501781831747

Weertman J (1974) Stability of the junction of an ice sheet and an ice shelf. *Journal of Glaciology* **13**(67), 3–11. doi: 10.3189/S0022143000023327

Zhang T, Price SF, Hoffman MJ, Perego M and Asay-Davis X (2020) Diagnosing the sensitivity of grounding-line flux to changes in sub-ice-shelf melting. *The Cryosphere* **14**(10), 3407–3424. doi: 10.5194/tc-14-3407-2020

APPENDIX A. Numerical confirmation

Figure 7 shows a comparison of equilibrium grounding-line positions for varying widths obtained with the different methods listed in Section 2.3.2. The grey area indicates a retrograde bed. Note that we can only find stable steady states with the numerical method, while we can calculate stable and unstable steady state with the analytical and semi-analytical methods described above. The semi-analytical and numerical results agree well with each other. The analytic results are a good match for the case of a constant ice-shelf length and a constant calving front position, but deviate from the case with a constant ice-shelf front. This is most likely due to the approximation of the ice thickness at the calving front with (19a)–(19c) which is valid in the limits of no and strong buttressing only.

The grounding-line positions obtained for large values of the ice-shelf width W correspond to the unconfined, unbuttressed limit. Generally, as the width W decreases, buttressing increases, leading to equilibrium grounding-line positions that are downstream of the unconfined limit. However, the shape of the W–x_g relationship is markedly different for different calving laws, as expected from other studies (Schoof and others, 2017; Haseloff and Sergienko, 2018).

APPENDIX B. Analytic ice-shelf solutions

B.1. Unconfined ice shelves with slope-dependent melting

To derive an analytic solution, it is convenient to non-dimensionalize (1b), $(3)_2$, (4c) and (17) by setting $x = L_0\ x^* + x_g$, $h = h_g h^*$, $u = q_g h_g^{-1} u^*$ and $\gamma_3 = q_g h_g^{-2} \gamma_3^*$. We neglect asterisks rightaway in equations and immediately integrate (1b) with (4c) (see e.g. MacAyeal and Barcilon, 1988; Schoof, 2007b), leaving the simplified ice-shelf system for $\epsilon = 0$:

$$\left.\begin{aligned} \eta h \left|\tfrac{\mathrm{d}u}{\mathrm{d}x}\right|^{1/n-1}\tfrac{\mathrm{d}u}{\mathrm{d}x} - h^2 = 0 \\ \tfrac{\mathrm{d}(uh)}{\mathrm{d}x} = \gamma^*(1-h)\left|\tfrac{\mathrm{d}h}{\mathrm{d}x}\right| \end{aligned}\right\} \text{ on } x \in (0,\ 1). \tag{B1}$$

with

$$\eta = \frac{4 q_g^{1/n}}{A^{1/n} L_0^{1/n} \rho_i g (1-\rho_i/\rho_w) h_g^{1+1/n}} \tag{B2}$$

the ratio between the scale of the extensional stress at the grounding line and the scale of the driving stress at the grounding line and the initial conditions (17):

$$u = 1, \quad h = 1 \text{ at } x = 0. \tag{B3}$$

Assuming $\mathrm{d}h/\mathrm{d}x < 0$, we can integrate $(B1)_2$ by use of (B3) which provides the ice velocity as a function of ice thickness

$$u = \left(1 + \frac{\gamma_3}{2}\right)\frac{1}{h} - \gamma_3 + \frac{\gamma_3}{2} h.$$

Using the product rule we can rewrite (B1) as an implicit integral equation for h:

$$\int_h^1 h^{-n-1}\left[\gamma_3(1-h) + u\right]\mathrm{d}h = -\eta^{-n}\int_x^0 \mathrm{d}x^*$$

which can be simplified to

$$\int_h^1 \frac{2 + \gamma_3 - \gamma_3 h^2}{2h^{n+2}}\,\mathrm{d}h = \eta^{-n} x.$$

Integration gives

$$\frac{2+\gamma_3}{2(n+1)}\left(h^{-(n+1)} - 1\right) - \frac{\gamma_3}{2(n-1)}\left(h^{1-n} - 1\right) = \eta^{-n} x \tag{B4}$$

and re-dimensionalization gives

$$\frac{2 + \gamma_3 \frac{h_g^2}{q_g}}{2(n+1)}\left[\left(\frac{h}{h_g}\right)^{-(n+1)} - 1\right] - \frac{\gamma_3 \frac{h_g^2}{q_g}}{2(n-1)}\left[\left(\frac{h}{h_g}\right)^{1-n} - 1\right] = \eta^{-n} x, \tag{B5}$$

for $h > 0,\ \gamma_3 \le 0$

The left-hand side of this equation is non-linear in h/h_g (see Fig. 8a), and solutions of this equation require $x = L_s/L_0 < 1$ below a critical $\gamma_3 = \gamma_c$. To find γ_c we determine the ice thickness $h = h_{crit}$ that minimizes (B4) by taking the derivative with respect to h. This gives

$$h_{crit} = \sqrt{\frac{2+\gamma_c}{\gamma_c}}.$$

Re-dimensionalization and substituting h_{crit} into (B5) gives

$$\begin{aligned} &\frac{2 + \gamma_c \frac{h_g^2}{q_g}}{2(n+1)}\left[\left(\frac{2 + \gamma_c \frac{h_g^2}{q_g}}{\gamma_c \frac{h_g^2}{q_g}}\right)^{-(n+1)/2} - 1\right] \\ &- \frac{\gamma_c \frac{h_g^2}{q_g}}{2(n-1)}\left[\left(\frac{2 + \gamma_c \frac{h_g^2}{q_g}}{\gamma_c \frac{h_g^2}{q_g}}\right)^{(1-n)/2} - 1\right] \\ &= \eta^{-n}. \end{aligned} \tag{B6}$$

For $n = 3$, it is possible to write solutions to (B5) in closed form, and the ice

https://doi.org/10.1017/jog.2022.29 Published online by Cambridge University Press

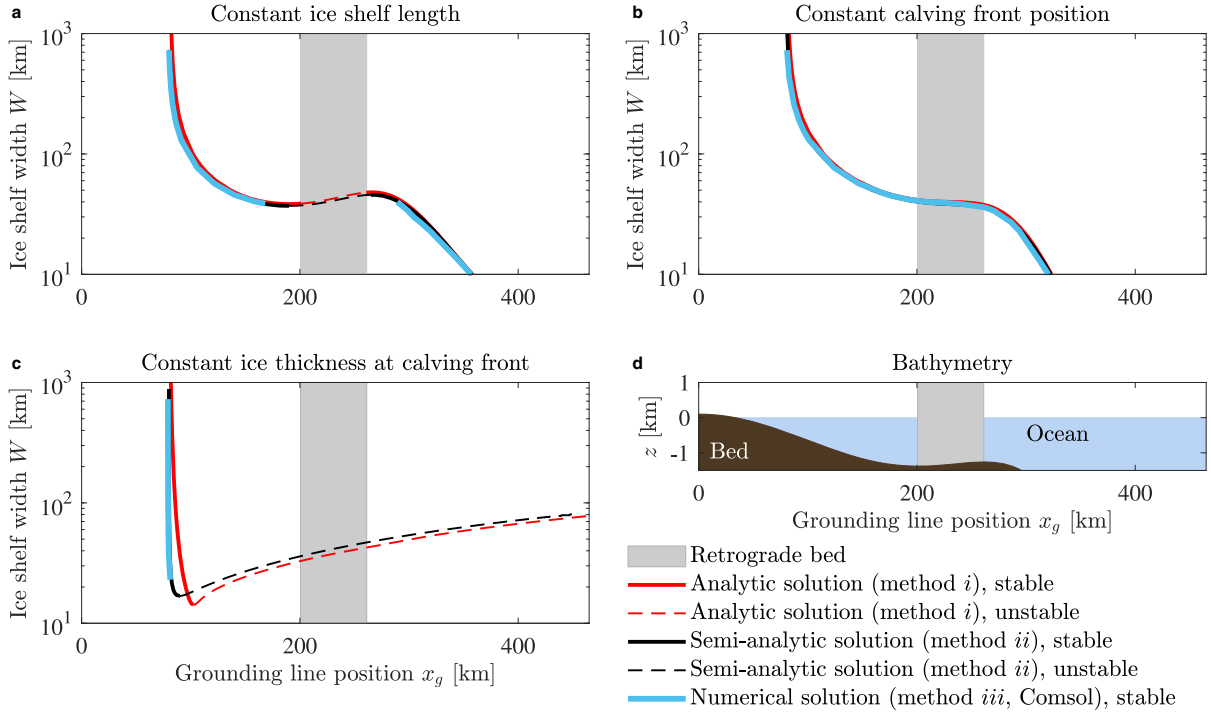

Fig. 7. Comparison of grounding line positions for different ice-shelf widths obtained with the different methods (*i*)–(*iii*) outlined in the text. Analytic results are obtained from solution of (10) with (14), semi-analytic results are obtained from solution of (10) with (22a)–(22c) and numerical results are obtained from solution of (1)–(4) with Comsol. The grey-shaded area marks the upward-sloping part of the bed. Panel a: grounding-line positions for different ice-shelf widths with prescribed ice-shelf length. Panel b: grounding-line positions for different ice-shelf widths with prescribed calving front position. Panel c: grounding-line positions for different ice-shelf widths with prescribed ice thickness at the calving front. Panel d: bed elevation.

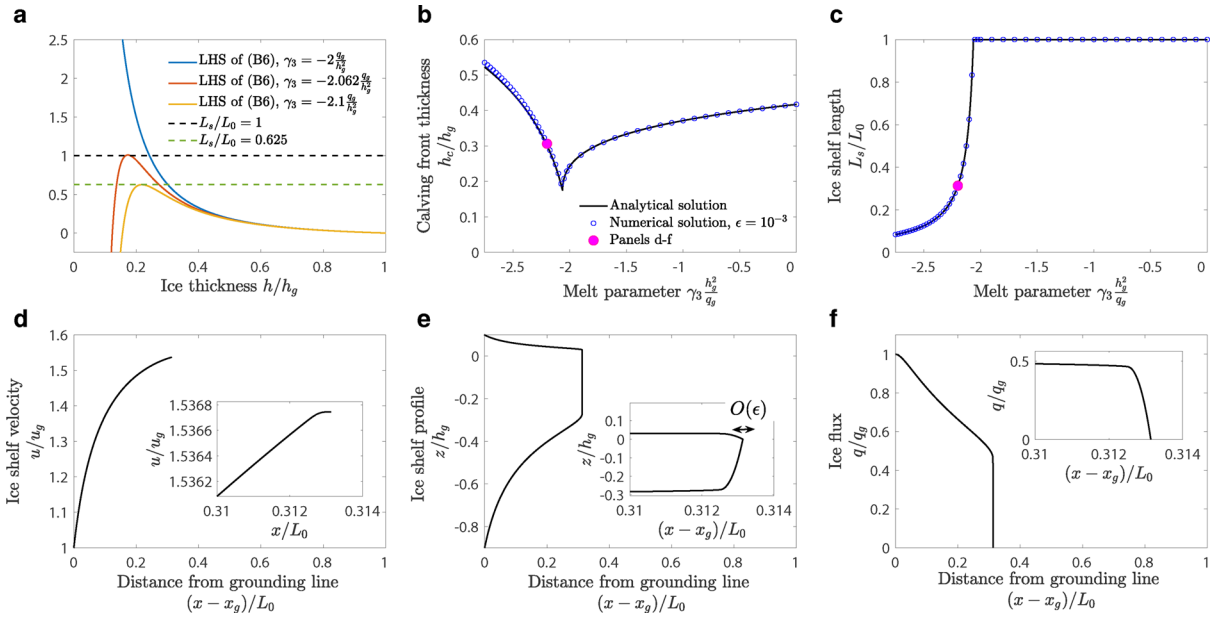

Fig. 8. Examples for unbuttressed profiles with slope-dependent melting $\dot{m} = \gamma_3(h_g - h)|dh/dx| \times (1 + \varepsilon^2(dh/dx)^2)^{-1/2}$. If $\gamma_3 < \gamma_c$, the ice thickness at the ice-shelf edge goes to zero over a short distance, as the melt rate becomes singular when $u = -\gamma_3(h_g - h)$.

thickness at the ice-shelf front is given by:

$$h_c = h_g \times \begin{cases} \sqrt{\frac{\gamma_3 h_g^2 q_g^{-1}}{\gamma_3 h_g^2 q_g^{-1} - 2 - 8\eta^{-3}} \pm \sqrt{\frac{\gamma_3^2 (h_g^2 q_g^{-1})^2}{(2+8\eta^{-3} - \gamma_3 h_g^2 q_g^{-1})^2} + \frac{\gamma_3 h_g^2 q_g^{-1} + 2}{2 + 8\eta^{-3} - \gamma_3 h_g^2 q_g^{-1}}} & \text{if } \gamma_c \le \gamma_3 \le 0 \\ \sqrt{\frac{2 + \gamma_3 h_g^2 q_g^{-1}}{\gamma_3 h_g^2 q_g^{-1}}}, & \text{if } \gamma_3 < \gamma_c. \end{cases} \quad \text{(B7)}$$

We compare these analytic solutions for the ice thickness at the ice-shelf front $h(x = 0) = h_c$ with numerical solutions in Figure 8, panels b and c. Note that we plot the 'apparent' ice thickness at the shelf front for solutions with $\epsilon > 0$ in panel b.

B.2. Grounding-line backstress for location-dependent melting $\dot{m} = f(x)$

To find solution for (23a), we closely follow Haseloff and Sergienko (2018), but assume a variable melt rate $\dot{m} = f(x)$. It is convenient to non-dimensionalize

https://doi.org/10.1017/jog.2022.29 Published online by Cambridge University Press

(1b), $(3)_2$, (4c) and (17) by setting $x = L_s x^* + x_g$, $h = h_g h^*$, $u = q_g h_g^{-1} u^*$ and $\dot{m} = q_g L_s^{-1} \dot{m}^*$. We neglect asterisks rightaway and obtain the non-dimensional system of ice-shelf equations

$$\eta(h|u|_x^{1/n-1}u_x)_x - \beta h|u|^{1/n-1}u - 2\,hh_x = 0 \tag{B8a}$$

$$(uh)_x = f(x) \tag{B8b}$$

with boundary conditions

$$h = u = 1 \text{ at } x = 0, \quad \text{and} \quad \eta h|u|_x^{1/n-1}u_x = h^2 \text{ at } x = 1 \tag{B8c}$$

where subscripts indicate derivatives. We have introduced the non-dimensional groups η and β

$$\eta = \frac{4q_g^{1/n}}{\rho g(1-\rho_i/\rho_w)A^{1/n}L_s^{1/n}h_g^{1/n+1}}, \quad \beta = \frac{2C_w q_g^{1/n}L_s}{\rho g(1-\rho_i/\rho_w)A^{1/n}W^{1/n+1}h_g^{1/n+1}}$$

and will assume $\eta \ll \beta \sim 1$, so that we can simplify (B8a):

$$-\beta h|u|^{1/n-1}u = 2\,hh_x. \tag{B9}$$

Integration of (B8b) with $(B8c)_1$ is straightforward:

$$u = \frac{1+\int_0^x f(x')\mathrm{d}x'}{h}. \tag{B10}$$

Using $M(x) = \int_0^x f(x')\,\mathrm{d}x'$ in (B9), we obtain:

$$-\frac{\beta}{2}|1+M(x)|^{1/n-1}(1+M(x))\,\mathrm{d}x = h^{1/n}\,\mathrm{d}h. \tag{B11a}$$

For the flux to remain positive over the length of the ice shelf, we require $(1 + M(x)) > 0$ for $0 < x \leq 1$. Requiring this, we can integrate once more

$$h(x) = \left[h_1^{1/n+1} + \beta\frac{1/n+1}{2}\int_x^1 \left(1+M(x')\right)^{1/n}\mathrm{d}x'\right]^{n/(n+1)} \tag{B12a}$$

where $h_1 = [\eta^n\beta(1+M(1))^{1/n+1}/2]^{n/(n+1)^2}$ is the ice thickness at the ice-shelf front (see Haseloff and Sergienko, 2018, for details). From (B12a) with (B10) we can obtain an expression for the ice-shelf velocities in the main ice-shelf body:

$$u(x) = \frac{1+\int_0^x f(x')\mathrm{d}x'}{\left[h_1^{1/n+1} + \beta\frac{n+1}{2n}\int_x^1(1+M(x'))^{1/n}\mathrm{d}x'\right]^{n/(1+n)}}. \tag{B12b}$$

This velocity has to match the reduction in buttressing experienced at the grounding line (again, see Haseloff and Sergienko, 2018, for details):

$$(1-\Theta)^{-1/2} = \lim_{x\to 0} u(x)$$

so that we obtain

$$\Theta = 1 - \lim_{x\to 0}\frac{\left[h_1^{1/n+1} + \beta\frac{n+1}{2n}\int_x^1[1+M(x)]^{1/n}\mathrm{d}x\right]^{2n/(n+1)}}{\left(1+\int_0^x f(x')\mathrm{d}x'\right)^2} \tag{B13a}$$

$$= 1 - \left[h_1^{1/n+1} + \beta\frac{n+1}{2n}\int_0^1 (1+M(x))^{1/n}\ \mathrm{d}x\right]^{2n/(n+1)}. \tag{B13b}$$

Note that $1 + M^*(x^*) = [q_g + \int_{x_g}^x f(x')\mathrm{d}x']/q_g = q(x)/q_g$. Re-dimensionalizing gives equation (23a).

APPENDIX C. Linear stability analysis

To perform a linear stability analysis, we use the time-dependent version of the reduced ice-sheet model (8) written in terms of h and $q = uh$

$$\gamma_w h^{m+1}q^{1/n} + \gamma_b q^m h^{1/n} + h^{m+1+1/n}(h+b)_x = 0 \tag{C1a}$$

$$h_t + q_x = \dot{a} \tag{C1b}$$

where subscripts indicate partial derivatives and we have introduced

$$\gamma_w = \frac{C_w}{\rho_i g A^{1/n}W^{1/n+1}}, \quad \text{and} \quad \gamma_b = \frac{C}{\rho_i g}.$$

The stress-continuity condition (13) with the backstress for a location-dependent melt rate $\dot{m}(x)$ (23a) becomes

$$\begin{aligned}\left[q_x h^{1/n+m+2} + q\left(\gamma_w q^{1/n}h^{m+1} + \gamma_b q^m h^{1/n} + h^{1/n+m+1}b_x\right)\right]^{1/n} = \\ = \frac{A^{1/n}}{2}h^{\frac{1/n+m+3-n}{n}}\left(\frac{1}{2}\rho g\delta h^2 - \alpha\left[\beta\left(q + \int_x^{x_c}\dot{m}\mathrm{d}x'\right)^{1/n}\right.\right. \\ \left.\left. + C_w\int_x^{x_c} q^{1/n}\mathrm{d}x'\right]^{2n/(n+1)}\right) \text{ at } x = x_g\end{aligned} \tag{C2}$$

where

$$\alpha = \frac{1}{2}\frac{\rho g\delta}{[(\rho g\delta)^n A W^{n+1}]^{2/(n+1)}}, \quad \beta = (4^n C_w)^{1/(n+1)}W, \quad \delta = 1-\rho_i/\rho_w$$

and h satisfies the floatation condition

$$h = -\frac{b}{1-\delta}, \quad \text{at } x = x_g$$

at the grounding line.

From the derivative of the floatation condition with respect to t we can also determine the rate of grounding-line migration:

$$\dot{x}_g = -\frac{h_t}{h_x + \frac{b_x}{1-\delta}} \tag{C3}$$

by substituting h_t from (C1b), and subsequently q_x from (13) into (C3) (note that we leave the buttressing term in its general form):

$$\dot{x}_g = \frac{A(\rho g\delta/4)^n h\Theta^n - \left(\gamma_w q^{1/n+1}h^{-1/n-1} + \gamma_b q^{m+1}h^{-m-2} + qh^{-1}b_x\right) - \dot{a}}{h_x + \frac{b_x}{1-\delta}}. \tag{C4}$$

To determine the stability of grounding-line positions obtained from (C2), we consider small time-dependent perturbations around steady-state solutions

$$\begin{aligned}h(x,t) = \hat{h}(x) + \varepsilon\tilde{h}(x,t), \quad q(x,t) = \hat{q}(x) + \varepsilon\tilde{q}(x,t), \\ x_g(t) = \hat{x}_g + \varepsilon\tilde{x}_g(t)\end{aligned} \tag{C5}$$

where ε is a small parameter. At leading order, the linearized perturbation problem recovers the steady-state outer problem (8) for $\hat{h}$ and $\hat{q}$. The linearized perturbation problem of $O(\varepsilon)$ is

$$\begin{aligned}\gamma_w\left(\frac{1}{n}\hat{h}^{m+1}\hat{q}^{1/n-1}\tilde{q} + (m+1)\hat{h}^m\hat{q}^{1/n}\tilde{h}\right) + \gamma_b\left(m\hat{q}^{m-1}\tilde{q}\hat{h}^{1/n} + \frac{1}{n}\hat{q}^m\hat{h}^{1/n-1}\tilde{h}\right) \\ + (m+1+1/n)\hat{h}^{m+1/n}\tilde{h}(\hat{h}+b)_x + \hat{h}^{m+1+1/n}\tilde{h}_x = 0\end{aligned} \tag{C6a}$$

$$\tilde{h}_t + \tilde{q}_x = 0. \tag{C6b}$$

https://doi.org/10.1017/jog.2022.29 Published online by Cambridge University Press

The perturbed flotation condition is

$$\tilde{h} + \tilde{x}_g \hat{h}_x = -\tilde{x}_g \frac{b_x}{1-\delta}. \tag{C7}$$

and the boundary conditions at the origin are

$$\tilde{q} = 0, \quad \tilde{h}_x = 0, \text{ at } x = 0. \tag{C8}$$

Equation (C2) is of the form

$$[\zeta(x, h, q, q_x)]^{1/n} = \frac{A^{1/n}}{2} h^{\frac{1/n+m+3-n}{n}} \left(\frac{1}{2} \rho g \delta h^2 - \alpha \left[\xi(x, h, q, x_c) \right]^{2n/(n+1)} \right)$$
$$\text{at } x = x_g \tag{C9}$$

To arrive to a linearized, perturbed version of (C2) we therefore start by recognizing that

$$\begin{aligned} \zeta^{1/n} = \hat{\zeta}^{1/n} + \varepsilon \frac{1}{n} \hat{\zeta}^{1/n-1} \Big[& (\tilde{h} + \hat{h}\tilde{x}_g) \frac{\partial \zeta}{\partial h} + (\tilde{q} + \hat{q}_x \tilde{x}_g) \frac{\partial \zeta}{\partial q} \\ & + (\tilde{q}_x + \hat{q}_{xx} \tilde{x}_g) \frac{\partial \zeta}{\partial q_x} + \frac{\partial \zeta}{\partial x} \tilde{x}_g \Big] + O(\varepsilon^2) \\ & \text{at } x = \hat{x}_g, \; h = \hat{h}(\hat{x}_g), \; q = \hat{q}(\hat{x}_g), \; q_x = \hat{q}_x(\hat{x}_g) \end{aligned} \tag{C10}$$

with $\hat{h}_x = \mathrm{d}\hat{h}/\mathrm{d}x$ and $\hat{q}_x = \mathrm{d}\hat{q}/\mathrm{d}x$ and

$$\hat{\zeta} = \hat{q}_x \hat{h}^{1/n+m+2} + \gamma_w \hat{q}^{1/n+1} h^{m+1} + \gamma_b \hat{q}^{m+1} \hat{h}^{1/n} + \hat{q} \hat{h}^{1/n+m+1} b_x. \tag{C11}$$

Introducing

$$\begin{aligned} A_1 &= \frac{1}{n} \hat{\zeta}^{1/n-1} \frac{\partial \zeta}{\partial q} \\ &= \frac{1}{n} \hat{\zeta}^{1/n-1} \left[\left(\frac{1}{n} + 1 \right) \gamma_w \hat{q}^{1/n} h^{m+1} + (m+1) \gamma_b \hat{q}^m \hat{h}^{1/n} + \hat{h}^{1/n+m+1} b_x \right] \end{aligned} \tag{C12a}$$

$$\begin{aligned} A_2 &= \frac{1}{n} \hat{\zeta}^{1/n-1} \frac{\partial \zeta}{\partial h} \\ &= \frac{1}{n} \hat{\zeta}^{1/n-1} \Big[(1/n + m + 2) \hat{q}_x \hat{h}^{1/n+m+1} + (m+1) \gamma_w \hat{q}^{1/n+1} \hat{h}^m \\ &\quad + \frac{1}{n} \gamma_b \hat{q}^{m+1} \hat{h}^{1/n-1} + (1/n + m + 1) \hat{h}^{1/n+m} \hat{q} b_x \Big] \end{aligned} \tag{C12b}$$

$$A_3 = \frac{1}{n} \hat{\zeta}^{1/n-1} \frac{\partial \zeta}{\partial q_x} = \frac{1}{n} \hat{\zeta}^{1/n-1} \hat{h}^{1/n+m+2} \tag{C12c}$$

$$A_4 = \frac{1}{n} \hat{\zeta}^{1/n-1} \frac{\partial \zeta}{\partial x} = \frac{1}{n} \hat{\zeta}^{1/n-1} \hat{q} \hat{h}^{1/n+m+1}. \tag{C12d}$$

the $O(\varepsilon)$-term on the left side of (C9) is

$$\begin{aligned} & \frac{1}{n} \hat{\zeta}^{1/n-1} \left[\frac{\partial \zeta}{\partial q} \tilde{q} + \frac{\partial \zeta}{\partial q_x} \tilde{q}_x + \frac{\partial \zeta}{\partial h} \tilde{h} + \left(\frac{\partial \zeta}{\partial x} + \frac{\partial \zeta}{\partial h} \hat{h}_x + \frac{\partial \zeta}{\partial q} \hat{q}_x + \frac{\partial \zeta}{\partial q_x} \hat{q}_{xx} \right) \tilde{x}_g \right] \\ & = A_1(\tilde{q} + \hat{q}_x \tilde{x}_g) + A_2(\tilde{h} + \hat{h}_x \tilde{x}_g) + A_3(\tilde{q}_x + \hat{q}_{xx} \tilde{x}_g) + A_4 b_{xx} \tilde{x}_g \\ & \text{at } x = \hat{x}_g, \; h = \hat{h}(\hat{x}_g), \; q = \hat{q}(\hat{x}_g), \; q_x = \hat{q}_x(\hat{x}_g). \end{aligned}$$

Before we can repeat similar steps for the right-hand side of (C9), we have to make a decision about the form of the calving law, which enters through ξ:

$$\xi = \beta \left(\hat{q}(x) + \int_x^{x_c} \dot{m}(x') \, \mathrm{d}x' \right)^{1/n} + C_w \int_x^{x_c} \left[\hat{q}(x) + \int_{x'}^{x_c} m(x'') \mathrm{d}x'' \right]^{1/n} \mathrm{d}x'.$$

Complex calving laws might depend on the ice thickness, flux, and grounding-line position, i.e. $x_c = x_c(x_g, \; h_g, \; q_g)$, see for example (6). If we allow for a general calving law like this, then (C9) is of the form

$$\begin{aligned} & A_1(\tilde{q} + \hat{q}_x \tilde{x}_g) + A_2(\tilde{h} + \hat{h}_x \tilde{x}_g) + A_3(\tilde{q}_x + \hat{q}_{xx} \tilde{x}_g) + A_4 b_{xx} \tilde{x}_g \\ & = B_1(\tilde{h} + \hat{h}_x \tilde{x}_g) - Bc_3 \left[\frac{\partial x_c}{\partial h} (\tilde{h} + \hat{h}_x \tilde{x}_g) + \frac{\partial x_c}{\partial q} (\tilde{q} + \hat{q}_x \tilde{x}_g) + \frac{\partial x_c}{\partial x_g} \tilde{x}_g \right] \\ & - Bc_1(\tilde{q} + \hat{q}_x \tilde{x}_g) + Bc_3 \tilde{x}_g \quad \text{at } x = \hat{x}_g \end{aligned} \tag{C13}$$

with

$$\begin{aligned} B_1 = & \left(\frac{1/n + m + 3 - n}{n} \right) \frac{A^{1/n}}{2} \hat{h}^{\frac{1/n+m+3-2n}{n}} \left(\frac{1}{2} \rho g \delta \hat{h}^2 - \alpha \hat{\xi}^{\frac{2n}{n+1}} \right) \\ & + \frac{A^{1/n}}{2} \hat{h}^{\frac{1/n+m+3-n}{n}} \rho g \delta \hat{h} \end{aligned} \tag{C14a}$$

$$B = \frac{A^{1/n}}{2} \hat{h}^{\frac{1/n+m+3-n}{n}} \alpha \frac{2n}{n+1} \hat{\xi}^{\frac{n-1}{n+1}}. \tag{C14b}$$

and

$$c_1 = \frac{\partial \xi}{\partial q} = \frac{\beta}{n} \hat{q}_c^{1/n-1} + \frac{1}{n} C_w \int_x^{x_c} \left[\hat{q}(x) + \int_{x'}^{x_c} m(x'') \mathrm{d}x'' \right]^{1/n-1} \mathrm{d}x' \tag{C15a}$$

$$c_2 = -\frac{\partial \xi}{\partial x} = \frac{\beta}{n} \hat{q}_c^{1/n-1} \dot{m}(x) + C_w \hat{q}_c^{1/n} \tag{C15b}$$

$$\begin{aligned} c_3 = \frac{\partial \xi}{\partial x_c} = & \frac{\beta}{n} \hat{q}_c^{1/n-1} \dot{m}(x_c) + C_w \hat{q}(x)^{1/n} \\ & + \frac{1}{n} C_w \dot{m}(x_c) \int_x^{x_c} \left(\hat{q}(x) + \int_{x'}^{x_c} \dot{m} \mathrm{d}x'' \right)^{1/n-1} \mathrm{d}x'. \end{aligned} \tag{C15c}$$

We also used

$$\hat{q}_c(\hat{q}, x_c) = \hat{q}(x) + \int_x^{x_c} \dot{m}(x') \, \mathrm{d}x'.$$

C.1 Sturm–Liouville form and general stability condition

To show that (C6)–(C8) with (C13) is a Sturm–Liouville problem for $\tilde{h}$, we assume the solution is separable, and can be written as $\tilde{h}(x, \; t) = \tilde{h}(x) \mathrm{e}^{\Lambda t}$, where Λ is an eigenvalue, whose sign determines the stability. From (C1b)

$$\tilde{q}_x = -\Lambda h, \text{ i.e. } \quad \tilde{q} = -\Lambda \int_0^{\hat{x}_g} \tilde{h} \, \mathrm{d}x \tag{C16a}$$

and from (C7)

$$\tilde{x}_g = -\frac{\tilde{h}}{\hat{h}_x + \frac{b_x}{1-\delta}}. \tag{C16b}$$

With a little algebra (largely following Sergienko and Wingham, 2022), we can thus rewrite (C6b) as

$$\left(P(x) \tilde{h}_x \right)_x - \left(Q(x) \tilde{h} \right)_x = \Lambda \tilde{h} \tag{C17}$$

with

$$P(x) = \frac{\hat{h}^{1/n+m+1}}{(\gamma_w/n) \hat{h}^{m+1} \hat{q}^{1/n-1} + m \gamma_b \hat{q}^{m-1} \hat{h}^{1/n}},$$
$$Q(x) = \frac{(\gamma_w/n) \hat{h}^m \hat{q}^{1/n} + \gamma_b (m+1) \hat{q}^m \hat{h}^{1/n-1}}{(\gamma_w/n) \hat{h}^{m+1} \hat{q}^{1/n-1} + m \gamma_b \hat{q}^{m-1} \hat{h}^{1/n}}.$$

It is straightforward to show that (C17) can be put into Sturm–Liouville form (again following Schoof, 2012; Sergienko and Wingham, 2022)

$$\left[\mu(x) P(x) \tilde{h}_x \right]_x - \mu(x) R(x) \tilde{h} = \Lambda \mu(x) \tilde{h}$$

https://doi.org/10.1017/jog.2022.29 Published online by Cambridge University Press

with μ an integrating factor and

$$\begin{aligned} R(x) &= [Q(x)]_x, \\ F(x) &= (P(x))_x - Q(x), \\ \mu(x) &= \frac{1}{P(x)} \exp\left(\int_0^x \frac{F(x')}{P(x')} \mathrm{d}x' \right). \end{aligned} \tag{C18}$$

For the boundary condition at the grounding line, we substitute (C16) into (C13) and divide by $\tilde{h}$, giving

$$\begin{aligned} &-\Lambda \left(\left[A_1 + B\left(c_1 + c_3 \frac{\partial x_c}{\partial q} \right) \right] \frac{\int \tilde{h} \mathrm{d}x}{\tilde{h}} + A_3 \right) \left(\hat{h}_x + \frac{b_x}{1-\delta} \right) \\ &= \left[A_1 + B\left(c_1 + c_3 \frac{\partial x_c}{\partial q} \right) \right] \hat{q}_x - \left[A_2 - B_1 + B c_3 \frac{\partial x_c}{\partial h} \right] \frac{b_x}{1-\delta} \\ &+ A_3 \hat{q}_{xx} + A_4 b_{xx} - B\left(c_2 - c_3 \frac{\partial x_c}{\partial x_g} \right) \end{aligned} \tag{C19}$$

As in Sergienko and Wingham (2022), the functions μ, P and R are continuous and μP is a positive function, and the boundary conditions (C8) and (C19) can be written as homogeneous function of $\tilde{h}$ and $\tilde{h}_x$. Importantly, as Sergienko and Wingham (2022) elaborate on, it is possible to show that for a Sturm–Liouville problem as the above, the eigenfunction corresponding to the largest eigenvalue does not change sign, provided $[A_1 + B(c_1 + c_3 \partial x_c/\partial q)] > 0$ (the parameter A_3 is positive by definition). A_1 is positive as long as $(\frac{1}{n}+1)\gamma_w \hat{q}^{1/n} h^{m+1} + (m+1)\gamma_b \hat{q}^m \hat{h}^{1/n} + \hat{h}^{1/n+m+1} b_x > 0$, $B > 0$ by definition, and the sign of $\partial x_c/\partial q$ depends on the calving law. If we reasonably assume that the steady solution is to remain grounded upstream of the grounding line, then $\hat{h}_x + b_x/(1-\delta) < 0$ (Schoof, 2012).

Under these circumstances, Eqn (C19) determines the stability of a grounding-line position determined from (13):

$$\text{if } \left[A_1 + B\left(c_1 + c_3 \frac{\partial x_c}{\partial q} \right) \right] > 0, \ \left(\hat{h}_x + \frac{b_x}{1-\delta} \right) < 0, \ \hat{\zeta} > 0$$

$$\text{then for } \begin{cases} \left(\left[A_1 + B\left(c_1 + c_3 \frac{\partial x_c}{\partial q_g} \right) \right] \hat{q}_x - \left[A_2 - B_1 + B c_3 \frac{\partial x_c}{\partial h_g} \right] \frac{b_x}{1-\delta} \right. \\ \left. + A_3 \hat{q}_{xx} + A_4 b_{xx} - B\left(c_2 - c_3 \frac{\partial x_c}{\partial x_g} \right) \right) < 0 \text{ stable} \\ \left(\left[A_1 + B\left(c_1 + c_3 \frac{\partial x_c}{\partial q_g} \right) \right] \hat{q}_x - \left[A_2 - B_1 + B c_3 \frac{\partial x_c}{\partial h_g} \right] \frac{b_x}{1-\delta} \right. \\ \left. + A_3 \hat{q}_{xx} + A_4 b_{xx} - B\left(c_2 - c_3 \frac{\partial x_c}{\partial x_g} \right) \right) > 0 \text{ unstable} \end{cases} \tag{C20}$$

where the third condition $\hat{\zeta} > 0$ has to be satisfied for steady-state solutions to exist. Note that the choice of the calving law enters through $\partial x_c/\partial h_g$, $\partial x_c/\partial x_g$ and $\partial x_c/\partial q_g$ which makes it possible for different calving choices to alter the stability of a steady state from stable to unstable.

C.2 Relationship with flux gradient

For comparison with the existing literature (Schoof, 2012; Sergienko and Wingham, 2022) it is convenient to express the stability condition as a function of the gradient of the grounding-line flux $\mathrm{d}q_g/\mathrm{d}x_g$. The stress condition (C2) provides the grounding-line flux for Θ given by (23a):

$$\begin{aligned} &\left[\dot{a} h_g^{1/n+m+2} + \gamma_w q_g^{1/n+1} h_g^{m+1} + \gamma_b q_g^{m+1} h_g^{1/n} + q_g h_g^{1/n+m+1} b_x \right]^{1/n} \\ &= \frac{A^{1/n}}{2} h_g^{\frac{1/n+m+3-n}{n}} \left(\frac{1}{2} \rho g \delta h_g^2 - \alpha \left[\beta \left(q_g + \int_{x_g}^{x_c} \dot{m} \mathrm{d}x' \right)^{1/n} \right. \right. \\ &\left. \left. + C_w \int_{x_g}^{x_c} \left(q_g + \int_{x'}^{x_c} \dot{m}(x'') \mathrm{d}x'' \right)^{1/n} \mathrm{d}x' \right]^{2n/(n+1)} \right). \end{aligned} \tag{C21}$$

Taking the derivative with respect to x_g and using the definitions of A_1–A_4 (C12), B and B_1(C14), evaluated at $x = x_g$, gives

$$\begin{aligned} &A_1 \frac{\mathrm{d}q_g}{\mathrm{d}x_g} + A_2 \frac{\mathrm{d}h_g}{\mathrm{d}x_g} + A_3 \frac{\mathrm{d}\dot{a}}{\mathrm{d}x_g} + A_4 \frac{\mathrm{d}^2 b}{\mathrm{d}x_g^2} = B_1 \frac{\mathrm{d}h_g}{\mathrm{d}x_g} \\ &- B \left\{ \frac{\beta}{n} \left(q_g + \int_{x_g}^{x_c} \dot{m} \mathrm{d}x' \right)^{1/n-1} \left(\frac{\mathrm{d}q_g}{\mathrm{d}x_g} + \dot{m}(x_c) \frac{\mathrm{d}x_c}{\mathrm{d}x_g} - \dot{m}(x_g) \right) \right. \\ &+ C_w q_g^{1/n} \frac{\mathrm{d}x_c}{\mathrm{d}x_g} - C_w q_c^{1/n} \\ &\left. + C_w \int_{x_g}^{x_c} \frac{1}{n} \left(q_g + \int_{x'}^{x_c} \dot{m} \, \mathrm{d}x'' \right)^{1/n-1} \left(\frac{\mathrm{d}q_g}{\mathrm{d}x_g} + \dot{m}(x_c) \frac{\mathrm{d}x_c}{\mathrm{d}x_g} \right) \mathrm{d}x' \right\}. \end{aligned} \tag{C22}$$

with

$$q_c = q_g + \int_{x_g}^{x_c} \dot{m}(x') \mathrm{d}x'.$$

Reordering gives:

$$\begin{aligned} &A_1 \frac{\mathrm{d}q_g}{\mathrm{d}x_g} - (B_1 - A_2) \frac{\mathrm{d}h_g}{\mathrm{d}x_g} + A_3 \frac{\mathrm{d}\dot{a}}{\mathrm{d}x_g} + A_4 \frac{\mathrm{d}^2 b}{\mathrm{d}x_g^2} \\ &= -B \left\{ \left(\frac{\beta}{n} q_c^{1/n-1} + \frac{1}{n} C_w \int_{x_g}^{x_c} \left(q_g + \int_{x'}^{x_c} \dot{m} \, \mathrm{d}x'' \right)^{1/n-1} \mathrm{d}x' \right) \frac{\mathrm{d}q_g}{\mathrm{d}x_g} \right. \\ &- \frac{\beta}{n} q_c^{1/n-1} \dot{m}(x_g) - C_w q_c^{1/n} \\ &\left. + \left(\frac{\beta}{n} q_c^{1/n-1} \dot{m}(x_c) + C_w q_g^{1/n} + \frac{1}{n} C_w \dot{m}(x_c) \int_{x_g}^{x_c} \left(q_g + \int_{x'}^{x_c} \dot{m} \, \mathrm{d}x'' \right)^{1/n-1} \mathrm{d}x' \right) \frac{\mathrm{d}x_c}{\mathrm{d}x_g} \right\} \end{aligned} \tag{C23}$$

with

$$\frac{\mathrm{d}x_c}{\mathrm{d}x_g} = \frac{\partial x_c}{\partial x_g} + \frac{\partial x_c}{\partial q_g} \frac{\mathrm{d}q_g}{\mathrm{d}x_g} + \frac{\partial x_c}{\partial h_g} \frac{\mathrm{d}h_g}{\mathrm{d}x_g}. \tag{C24}$$

We can identify $\mathrm{d}h_g/\mathrm{d}x_g = -b_x/(1-\delta)$, $\hat{q}_x = q_x = \dot{a}$, $\hat{q} = q_g$, $\hat{h} = h_g$, $b_{xx} = \mathrm{d}b_x/\mathrm{d}x_g$, $\hat{q}_{xx} = \mathrm{d}\dot{a}/\mathrm{d}x_g$ so that the stability condition (C19) is linked to the flux gradient through

$$\begin{aligned} &-\Lambda \left(\left[A_1 + B\left(c_1 + c_3 \frac{\partial x_c}{\partial q} \right) \right] \frac{\int h \, \mathrm{d}x}{\tilde{h}} + A_3 \right) \left(\hat{h}_x + \frac{b_x}{1-\delta} \right) \\ &= \left(A_1 + B\left(c_1 + c_3 \frac{\partial x_c}{\partial q} \right) \right) \left(\dot{a} - \frac{\mathrm{d}q_g}{\mathrm{d}x_g} \right) \end{aligned} \tag{C25}$$

and we can write (C20) as

$$\text{if } \left[A_1 + B\left(c_1 + c_3 \frac{\partial x_c}{\partial q} \right) \right] > 0, \ \zeta > 0, \ \left(\hat{h}_x + \frac{b_x}{1-\delta} \right) < 0$$

$$\text{then for } \begin{cases} \frac{\mathrm{d}q_g}{\mathrm{d}x_g} > \dot{a} & \text{stable} \\ \frac{\mathrm{d}q_g}{\mathrm{d}x_g} < \dot{a} & \text{unstable.} \end{cases} \tag{C26}$$

The same analysis can be applied to stability conditions derived by Sergienko and Wingham (2022) and reduce them to the form (C26).

https://doi.org/10.1017/jog.2022.29 Published online by Cambridge University Press